

# Strain activated - Single Photon Emissions in hBN: Effects of varying layer count

Utkarsh

A thesis presented for the partial fulfillment of Dual Degree in  
Engineering Physics (M. Tech + B. Tech)



Department of Physics  
Indian Institute of Technology  
Mumbai, India  
October 31, 2023

Supervisor: Prof. Anshuman Kumar  
Laboratory of Optics of Quantum Materials (LOQM)

# Abstract

Single Photon Emitters in 2D-materials provide numerous advantages for integrated photonics and quantum communication especially in hBN. The wide band-gap material hosts deep defects that produce stable SPEs at room temperature and being a 2D material, allows for control over the emission wavelength( $\sim 65$  meV) via strain tunability. Here we present a study of SPEs in hBN for varying crystal thickness, strain tuned by an array of gold nanopillars(height  $\sim 100$  nm) lithographed on a layer of SiO<sub>2</sub>(300 nm on Si substrate). The photoluminescence of SPEs present at varying hBN thicknesses and corresponding photon antibunching measurements and lifetimes are studied. Theoretical understanding of the origin of these SPEs and effects of strain and gold LSPRs is presented.

# Contents

<b>1</b>	<b>Introduction</b>	<b>7</b>
1.0.1	Bulk v/s surface SPEs . . . . .	8
1.0.2	Desired properties of SPEs . . . . .	9
1.1	$g^{(2)}$ . . . . .	10
1.2	Fluorescence Lifetime Measurement . . . . .	11
<b>2</b>	<b>Theory</b>	<b>13</b>
2.1	hBN Basics . . . . .	13
2.1.1	Photoluminescence of defect states . . . . .	13
2.2	Three level model for PL spectra . . . . .	17
2.2.1	How does strain help? . . . . .	21
<b>3</b>	<b>Experiments</b>	<b>27</b>
3.1	Sample Preparation . . . . .	27
3.1.1	Nitto Blue tape exfoliation . . . . .	27
3.2	Sample Characterisation . . . . .	28
3.3	hBN Transfer on Gold Nanocones . . . . .	28
<b>4</b>	<b>Lumerical Simulations</b>	<b>37</b>
4.1	Surface Plasmon Resonance . . . . .	37
4.2	Periodic array of nanocones - no hBN . . . . .	39
<b>5</b>	<b>Conclusion</b>	<b>42</b>
5.0.1	Future Work . . . . .	42
<b>A</b>	<b>Further Work</b>	<b>ii</b>
A.0.1	UV-Ozone Treatment . . . . .	ii
A.0.2	Reflectance Spectrum . . . . .	iv

# List of Figures

1.1	hBN defects [1] . . . . .	8
1.2	Photon detections as a function of time for a) antibunched, b)random, and c) bunched light . . . . .	11
1.3	Hanbury Brown and Twiss (HBT) Experiment Setup . . . . .	12
1.4	TCSPC Setup . . . . .	12
2.1	Configuration coordinate diagram for a two level system . . . . .	14
2.2	Luminescence lineshapes of three model defects. (a) Weak electron-phonon coupling (Huang-Rhys factor $S = 0.3$ ). (b) Intermediate electron-phonon coupling ( $S = 5.0$ ). (c) Strong electron-phonon coupling ( $S = 15.0$ ). The ZPL is indicated with a (red) arrow. Solid line shows the actual luminescence lineshape, and the dashed line shows a calculation based on a one-dimensional configuration coordinate diagram (“1D model”). A comparison can be made between this figure and Fig.(2.3) where the two cases have $S \sim 1$ and $S < 1$ respectively.	16
2.3	Examples of Group-1 and Group-2 visible SPE observed from h-BN defects (black points), and their fits to extrapolated Huang-Rhys models (red lines), using Lorentzian line profiles of specified FWHM. The fits are characterised by their total Huang-Rhys factors, Debye-Waller factors, and reorganization energies, with spectral features labelled as the ZPL (0-0), the primary PSB (0-1), and overtone PSBs (0-2, 0-3, etc.) . . . . .	17
2.4	(a) Schematic representation of spontaneous emission from a non-resonantly driven 2-level system. (b) The second order correlation function for a 2-level system, $g(2)(\tau)$ . (c) Schematic representation of spontaneous emission from a non-resonantly driven 3-level system. (d) The second order correlation function for a 3-level system. . . . .	20
2.5	P=0 Height Profile . . . . .	23
2.6	Uniaxial tensile strain values as a function of the nano-pillar radius, calculated at the topmost edge of the nano-antenna ( $H = 200$ nm) for both single and double layer WSe <sub>2</sub> . . . . .	23
2.7	Conduction band potential minimum ( $V_c b$ ), calculated for the K(K') point of the Brillouin zone, for both single (1L) and double (2L) layer WSe <sub>2</sub> , relative to the height profile shown in Fig. (2.5) . . . . .	24
2.8	Strain v/s nano-pillar radius for the three pressure models . . . . .	25
2.9	Radial charge localisation around the nanopillar geometry plotted alongside the nanopillar geometry and the conduction band profile. . . . .	26

3.1	Nitto Blue Tape Exfoliation : Exfoliated Samples. Almost no tape residue on the PDMS substrate and hBN samples. Flake sizes are much larger than $10\mu m$ . The monolayers obtained lie in the size range of $10\mu m - 20\mu m$ in diameter . . . . .	28
3.2	(a) Positions where the Raman spectra was taken. (b) Corresponding Raman spectra, showing the effect of change of layer count on the Raman spectra, clearly indication the hBN Raman peak $\sim 1365cm^{-1}$ , along width a PDMS peak. . . . .	28
3.3	The lithographed gold nanocones [height $\sim 100nm$ ] on SiO <sub>2</sub> [ $\sim 300nm$ ] on a Si substrate, with the diameter and periodicity marked. . . . .	29
3.4	Simulation of the geometry of a single nanocone . . . . .	29
3.5	A transferred hBN sample on the periodic nanocone structure. Residue due to PDMS is visible on the nanocones. . . . .	30
3.6	The clear peaks at $\sim 1365cm^{-1}$ indicates the success of the transfer process . . . . .	30
3.7	. . . . .	31
3.9	Caption . . . . .	32
4.1	Caption . . . . .	38
4.2	Cross-section field amplitude and reflected field amplitude at $\lambda = 536nm$ . . . . .	40
4.3	Cross-section field intensity and reflected field intensity at $\lambda = 536nm$ . . . . .	41
A.2	Reflectance Spectra . . . . .	iv

# List of Tables

2.1 Pressure Models . . . . .	22
-------------------------------	----

# Chapter 1

## Introduction

Single photon states [2] are defined as a photon number state with number of photons = 1 at every point in time. In terms of photon creation and annihilation operators, that emerge from second quantization of the electro-magnetic field, we get  $\hat{a}^\dagger \hat{a} |\Psi\rangle = |\Psi\rangle$ . These definitions are closely related to the photon emission statistics, which can be used to identify single photon sources.

Single photon emitters (SPEs) [3] are an essential component of quantum technologies, such as quantum communication, quantum computing, and quantum sensing. SPEs in hexagonal boron nitride (hBN) [4][5][6][1] have attracted significant interest due to their excellent photostability, narrow linewidth, and room temperature operation. In particular, strain tuning of SPEs in hBN[7][5] has emerged as a promising method to enhance their performance by tuning the local electronic and vibrational states.

Hexagonal boron nitride is a wide-bandgap insulator [8] with a layered structure that consists of stacked two-dimensional (2D) honeycomb lattices of boron and nitrogen atoms. Defects in the hBN lattice, such as nitrogen-vacancy centers (NV centers) or boron-vacancy centers (BV centers), can act as SPEs[9]. These defects result from vacancies or substitutions of boron or nitrogen atoms in the hBN lattice, leading to localized electronic and vibrational states that can efficiently emit single photons.

The properties of SPEs in hBN can be tuned by introducing strain, which modifies the local environment of the defect. Strain can be induced by various methods, such as bending, twisting, or applying pressure to the hBN sample. Strain can also be introduced by depositing hBN on a substrate with a different lattice constant, such as graphene or mica.

Strain tuning of SPEs in hBN has several advantages over other methods of tuning SPEs, such as magnetic[10] or electric fields[11]. First, strain does not introduce additional noise or decoherence to the quantum state of the SPE, unlike external fields. Second, strain can be locally applied to specific defects, allowing for the precise tuning of individual SPEs. Third, strain can be dynamically controlled, enabling the tuning of SPEs in real-time[12].

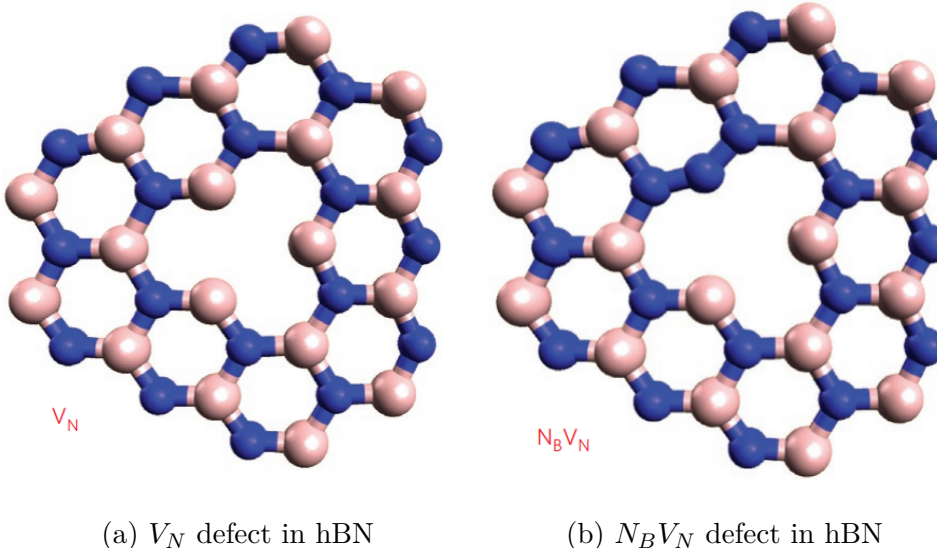


Figure 1.1: hBN defects [1]

Several studies have demonstrated the strain tuning of SPEs in hBN. For example, researchers have shown that the emission wavelength of NV centers in hBN can be redshifted by up to 20 nm by applying strain using a micromanipulator. The strain-induced redshift is attributed to the modulation of the electronic structure of the NV center, resulting in a change in the energy levels of the defect. Similarly, BV centers in hBN have been shown to exhibit a blueshift in their emission wavelength under strain, which is also attributed to the modification of the electronic and vibrational states of the defect.

Furthermore, strain tuning of SPEs in hBN can be combined with other techniques, such as resonant excitation or plasmonic enhancement, to further enhance their performance. For example, researchers have demonstrated that the coupling between NV centers in hBN and a plasmonic nanoantenna can be enhanced by up to 30 times by introducing strain to the hBN sample. This coupling enhancement is attributed to the change in the local environment of the NV center, resulting in a stronger interaction with the plasmonic field, due to charge trapping which will be discussed in a later section.

In summary, strain tuning of SPEs in hBN is a promising method to enhance their performance for various quantum technologies. The ability to dynamically control the strain and locally tune individual SPEs makes this approach particularly attractive for practical applications.

### 1.0.1 Bulk v/s surface SPEs

Monolayer SPEs in hBN have attracted significant interest due to their excellent photostability and narrow linewidth, making them promising candidates for use in quantum technologies. Monolayer hBN has a thickness of only one atomic layer, which results in a reduced interaction between the SPEs and the hBN lattice. This leads to a longer coherence time and a higher quantum yield compared to bulk SPEs in hBN.

Bulk SPEs in hBN have a higher probability of interacting with the hBN lattice, leading to increased non-radiative recombination and decreased quantum yield compared to monolayer SPEs. Bulk hBN can also have a higher concentration of defects, which can lead to spectral broadening and reduced coherence times of the SPEs. However, the emission wavelengths of bulk SPEs in hBN can be more stable over time compared to monolayer SPEs due to their stronger interaction with the surrounding lattice.

Furthermore, the properties of SPEs in hBN can be tuned by introducing strain or doping, which can have different effects on monolayer and bulk SPEs. For example, strain tuning of SPEs can lead to a redshift in the emission wavelength of monolayer SPEs in hBN, while bulk SPEs exhibit a blueshift. Doping can also have different effects on the properties of SPEs in monolayer and bulk hBN, with monolayer SPEs showing a more significant increase in quantum yield compared to bulk SPEs.

### **Effect of thickness of hBN on SPE properties**

The thickness of hexagonal boron nitride (hBN) crystals can have a significant effect on the properties of single photon emitters (SPEs) in hBN. The thickness of the hBN crystal can affect the electronic and vibrational states of the defects that act as SPEs, leading to changes in the emission wavelength, linewidth, and quantum yield of the SPEs.

Several studies have investigated the effect of the hBN thickness on the properties of SPEs. For example, one study demonstrated that the emission wavelength of NV centers in hBN shifts to longer wavelengths as the thickness of the hBN crystal increases. The redshift in the emission wavelength is attributed to the increase in the crystal field splitting energy of the NV center, which is proportional to the thickness of the hBN crystal. Another study showed that the linewidth of NV centers in hBN increases with increasing thickness, which is attributed to the increased interaction between the NV center and the hBN lattice as the thickness increases.

The thickness of the hBN crystal can also affect the quantum yield of SPEs. One study demonstrated that the quantum yield of NV centers in hBN decreases as the thickness of the hBN crystal increases. The decrease in quantum yield is attributed to the increased non-radiative recombination of excited states in thicker hBN crystals due to the increased interaction between the NV center and the hBN lattice.

Furthermore, the thickness of the hBN crystal can affect the stability of SPEs. One study demonstrated that the photostability of NV centers in hBN decreases as the thickness of the hBN crystal increases. The decrease in photostability is attributed to the increased interaction between the NV center and the hBN lattice, leading to a higher probability of the NV center being damaged by photobleaching or photo-induced defect formation..

#### **1.0.2 Desired properties of SPEs**

Finding all desired features in one system is a major challenge, and currently no solid-state system possess all of these properties. Desired are: the need to operate at room temperature, weak environmental interactions as these could cause dephasing and spectral diffusion, operation on demand, photostability without blinking, and

to emit photons with high efficiency and tightly controlled properties such as photon energy, polarization, lifetime, and the excited-state lifetime (the time required for their production following stimulation). An important associated quantitative measure is the quantum efficiency  $QE$  representing the fraction of emitted photons relative to the number of photons adsorbed. Values of  $QE \sim 1$  indicate that the SPEs efficiently respond to stimulation, rather than dissipating the absorbed energy by other means. Emitted light will always span some energy range, with typically the most intense emission being through the ZPL, with other phonons being emitted at lower energies through the PSB. The Deybe-Waller factor of the emitter,  $\alpha$  is the fraction of photons emitted in the ZPL and therefore provides a key indication as to how reproducible the emission is and hence how useful the SPE would be for device applications. The full-width at half maximum (FWHM) of the ZPL is a related key indicator.

## 1.1 $g^{(2)}$

In quantum optics, correlation functions are used to characterize the statistical and coherence properties of an electromagnetic field. The  $g^{(1)}$  function gives a measure of coherence between fields as:

$$g^{(1)}(\mathbf{r}_1, t_1; \mathbf{r}_2, t_2) = \frac{\langle E^*(\mathbf{r}_1, t_1) E(\mathbf{r}_2, t_2) \rangle}{[\langle |E(\mathbf{r}_1, t_1)|^2 \rangle \langle |E(\mathbf{r}_2, t_2)|^2 \rangle]^{\frac{1}{2}}} \quad (1.1)$$

The first-order correlation function  $g^{(1)}$ , which governs the visibility of interference fringes, has an intensity analogue called  $g^{(2)}$ . While  $g^{(2)}$  quantifies the intensity variations,  $g^{(1)}$  quantifies how the electric field changes over time.  $g^{(2)}$  is frequently referred to as the level of second-order coherence.

For a beam of light of intensity  $I(t)$ , the second-order correlation function (or degree of second-order temporal coherence)  $g^{(2)}$ , defined as

$$g^{(2)}(\tau) = \frac{\langle I(t)I(t+\tau) \rangle}{\langle I(t) \rangle^2} \quad (1.2)$$

From an experimental standpoint, we can rewrite this traditional definition of  $g^{(2)}$  as:

$$g^{(2)}(\tau) = \frac{\langle n(t)n(t+\tau) \rangle}{\langle n(t) \rangle^2} \quad (1.3)$$

This is because the number of counts  $n(t)$  registered on a photon-counting detector is proportional to the intensity of the impinging beam.

$g^{(2)}$  can be viewed as providing an answer to the following query: I've detected a photon at time  $t$ . What is the probability of detecting another photon at time  $t+\tau$ ?".

The amount of correlation between the number of photons discovered at time  $t$  and at time  $t+\tau$  is provided more specifically by  $g^{(2)}$ . This reveals how much the knowledge of what I will measure at time  $t+\tau$  translates into the knowledge of the number of photons at time  $t$ .

$g^{(2)}(0)$ : what does it mean to ask how many photons will be measured at time  $t+0=t$  if I have measured  $n$  photons at time  $t$ ? It can be considered as the limit of the number of photon counts at a very small time after  $t$ .

According to the second-order correlation function, light can be divided into three categories as follows:

Coherent light:  $g^{(2)}(0)>1$ , bunched light:  $g^{(2)}(0)=1$ , and antibunched light:  $g^{(2)}(0)<1$

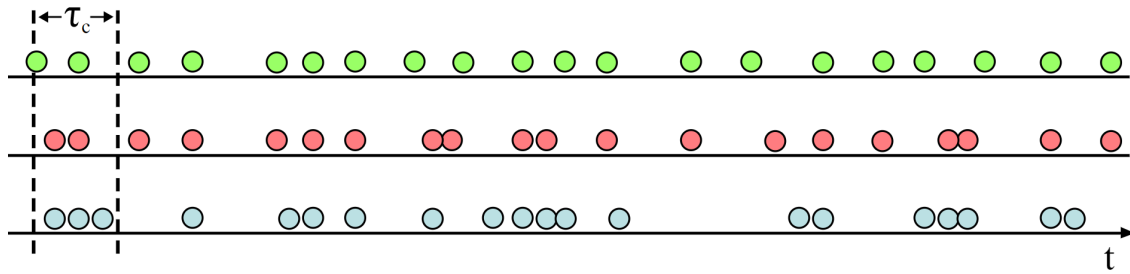


Figure 1.2: Photon detections as a function of time for a) antibunched, b)random, and c) bunched light

The number of photon counts for coherent light, such as that produced by a laser, is proportional to the intensity, which is by definition constant throughout time. As a result,  $g^{(2)}=1$  for any  $\tau$  and the number of counts at periods  $t$  and  $t+\tau$  are uncorrelated. Note that the average number of counts are generally not uncorrelated, and in the example of a beam with a constant intensity, average counts are constant. However, there is no correlation between the intensities' changes. This implies that one will never be able to minimize the uncertainty of the intensity fluctuations at time  $t+dt$ , regardless of how well one understands the distribution of intensities at time  $t$ .

Now,  $g^{(2)}(0)$  explains how frequently we notice two photons occasionally passing very close to one another (we imagine here always to detect one or zero photons at a time). While the two detection events are uncorrelated for coherent light, intensity changes on the source might cause detection events to occasionally be closer together for light coming from other types of classical sources, such as chaotic light. One talks about "bunched light" in these situations. As a result, there is a greater likelihood of another detection event occurring at times near  $t$  when there is a detection event at time  $t$ . Therefore, these sources meet  $g^{(2)}(0)>1$ . It can be demonstrated that classical light sources must constantly satisfy  $g^{(2)}(0) \geq g^{(2)}(\tau) \geq 1$ . This means that  $g^{(2)}(0) < 1$ , or antibunched light, is not feasible in the classical conception of light.

## 1.2 Fluorescence Lifetime Measurement

Time-correlated single-photon counting (TCSPC) is a well-known and widely used method for fluorescence lifetime measurements.

TCSPC requires The detection of single photons and the determination of their arrival times relative to a reference signal—typically the light source. A high rep-

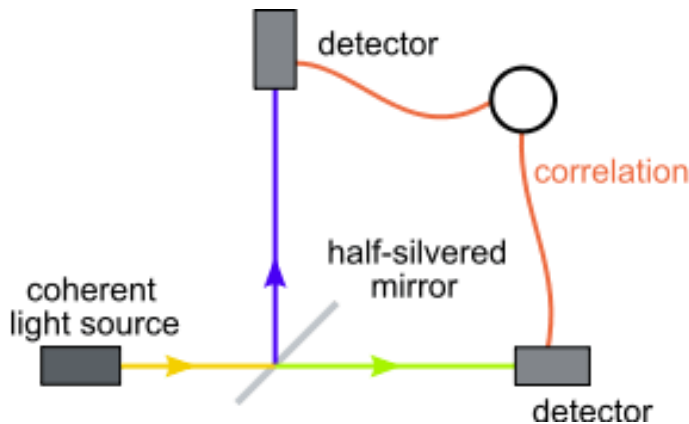


Figure 1.3: Hanbury Brown and Twiss (HBT) Experiment Setup

A coherent light source is necessary for TCSPC's statistical approach to collect enough photon events to provide the required precision in statistical data.

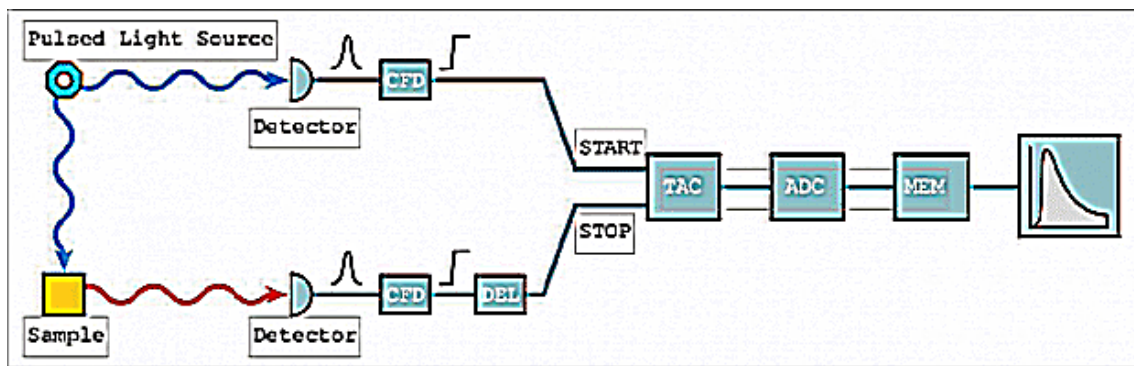


Figure 1.4: TCSPC Setup

A START and STOP signal pulses are used. An increase in a memory value in a histogram, where the channels on the x-axis reflect time, will be used to represent the length of time measured for one START - STOP sequence. A light source with a high repetition rate allows for the quick measurement of millions of START-STOP sequences. The fluorescence intensity vs time will be represented by the resulting histogram counts versus channels.

A pulse produced by a single photon is typically one of the inputs to the TCSPC electronics (either START or STOP). Photodetectors with intrinsically high gain can find single photons, e.g. avalanche photodiodes, photomultipliers, etc. It's crucial to make sure that each single photon event is recorded for statistical reasons. Multi-photon events will have an impact on the statistics of the histogram and will lead to inaccurate measurement findings. (This is referred to as the "pulse pile-up problem" in literature.) The photon rate is kept low in relation to the rate of the exciting lamp, often 5% or lower, to ensure that only one photon per light flash is detected.

# Chapter 2

## Theory

### 2.1 hBN Basics

hBN is a wide bandgap( $\sim 6\text{eV}$ ) semiconductor. Doping the same lattice structure as graphite, with Boron and Nitrogen for the two sublattices typical in graphene, there exist van der Waals interaction between the hexagonal layers. Since the van der Waals forces arise from induced dipole -induced dipole interactions, they are much weaker, while the in-plane interactions are strong enough. This allows for exfoliation of the layers, through scotch/nitto tape, first done to obtain graphene by Geim and Novoselov. hBN exhibits an indirect bandgap of 6.08 eV in multilayer/bulk phase, while transitions to a direct bandgap of 6.47 eV in the monolayer [8]. Like any other crystal structure, hBN can host defect sites, of various types including but not limited to vacancies( $V_N$ ,  $V_B$ ), impurities(e.g. carbon) and dislocation coupled with a vacancy( $N_B V_B$ ). These defects can be naturally occurring or can be incorporated externally for example, by ion irradiation, introduction of oxygen plasma and annealing, which we also experimented with. The exciting property of these defects in hBN is due to the presence of a large bandgap. The large bandgap allows for presence deep defect levels within the bandgap, which remain relatively unoccupied at room temperature, since the thermal energy is not sufficient to excite electrons in these states. Luckily, the defects in hBN allow for deep levels in the bandgap. Thus transitions between these levels can be controlled by external illumination, and the corresponding emission studied, allowing for stable emissions at room temperature. These emissions from inter-defect levels gives SPEs, since these are localised defects, and thus two defects act as a two level system. In either, bulk, or monolayer hBN, the direct or indirect nature of the bandstructure doesn't play a role for SPEs, since only the defect levels contribute to them.

Although several colour centres have been proposed so far, despite the research efforts made to identify the origin of SPE in h-BN, further detailed investigations are needed to unveil the origin of this emission.

#### 2.1.1 Photoluminescence of defect states

Absorption and emission of light transfers the defect from one state to another. The defect states are coupled to the atomic structure of the lattice. Thus the emission

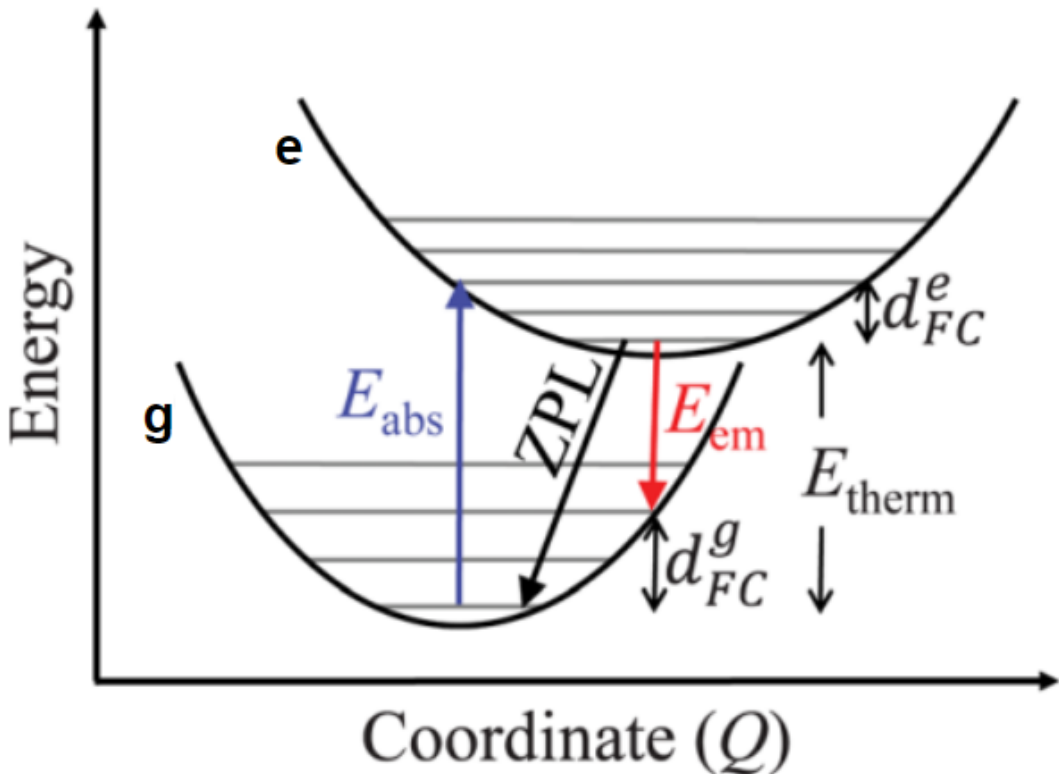


Figure 2.1: Configuration coordinate diagram for a two level system

and absorption can be studied best with the *configuration coordinate diagrams* as shown in Fig(2.1).

The wavefunction of a defect can be either delocalized or localized. If it is delocalized, then the electron density is very low at the defect and does not exert much influence on the atomic positions. This is the case for shallow defects. If the wavefunction is localized (on the defect itself and/or a few neighboring atoms), then this has a strong effect on how the atoms rearrange themselves locally when the charge of the defect changes or, more generally, when the electronic state of the defect changes. We study these deep, localised defects.

Consider two deep localised defect states. These can for example originate from a vacancy, thus creating a potential well which can have two bound levels below the continuum of energy states. The corresponding configuration coordinate diagram is shown below.

The defect state is described by the configuration coordinate(cc)  $Q$ , which, in a simple picture, is proportional to the bond length. At equilibrium, the energy of the level  $E$  is minimised at a particular  $Q$  value. To first order, the defect behaves like a harmonic oscillator i.e.,  $E \propto Q^2$ . A photon excites the electron from the ground state ' $g$ ' to the first excited state ' $e$ '. In the classical Frank-Condon expression, the transition happens instantaneously, i.e., during the transition the lattice positions do not change. Thus the energy levels do not change. The excited state has a different equilibrium position. Since the electron energy is increased, the bond strength has increased and thus the equilibrium coordinate  $Q$  for the excited state is larger than

for the ground state. The amount of energy absorbed in excitation is called the absorption energy, or excitation energy ( $E_{abs}$ ). The excited electron relaxes back to the minimum energy in the excited state, and this change in energy is called the absorption reorganisation energy, or the Frank-Condon shift  $d_{FC}^e$ .

The energy difference between the minimum energies of the ground and excited states is called the Zero Phonon Line or  $E_{ZPL}$  and is given by,

$$E_{ZPL} = E_{abs} - d_{FC}^e$$

Once in the excited state, the electron can relax to the ground state by emitting a photon of energy  $E_{em}$ . Under the same Frank-Condon approximation, the energy levels do not change during the transition. Finally the electron relaxes to the minimum energy in the ground state with a change in energy called emission reorganisation energy  $d_{FC}^g$ . Because of relaxations in the excited state and the ground state, the emission energy is lower than the absorption energy. The total energy difference between absorption and emission is called the Stokes shift. We see that the Stokes shift is given by the sum of Franck-Condon shifts in the ground and excited state

$$E_{abs} - E_{em} = d_{FC}^e + d_{FC}^g$$

Now, to understand the effect of phonons, consider the vibrational levels(grey lines) present in the cc diagram(Fig.(2.1)). These levels are representative of the thermal vibrations of the lattice and thus the change in energy of the system in different modes of vibrations of the lattice. The spacing between these levels is proportional to  $\omega_e$  for the excited state, and  $\omega_g$  for the ground state. An important parameter in the study of the effect of phonons on the optical spectra is the *Huang-Rhys factor*  $S$ , which for the case  $\omega_e = \omega_g = \omega_o$  turns out to be:

$$S = \frac{d_{FC}}{\hbar\omega_0} \quad (2.1)$$

Essentially, the Huang-Rhys factor quantifies the number of phonons taking part in the excitation or emission process.

**Emission Line Shape** Within the 1D model, the normalized luminescence line-shape is given by:

$$L(\hbar\omega, T) = \sum_{n,m} w_m(T) |\langle \chi_{em} | \chi_{gn} \rangle|^2 \delta(E_{ZPL} + m\hbar\omega_e - n\hbar\omega_g - \hbar\omega) \quad (2.2)$$

The sum runs over all vibrational levels in the excited state (m) and the ground state (n).  $w_m(T)$  is the thermal occupation factor. In principle, at low temperatures ( $m = 0$ ), Eq. (6) describes a series of equidistant peaks: the emission of a photon without any phonons ( $n = 0$ ) is the ZPL, while the  $n = 1, 2, 3\dots$  peaks are referred to as phonon replicas.

Equation (6) corresponds to the quantum variant of the Franck-Condon approximation, which assumes that the transition dipole moment that describes the coupling between the excited state and the ground state does not depend on  $Q$ .  $\langle \chi_{em} | \chi_{gn} \rangle$  are Franck-Condon overlap integrals between vibrational levels in the ground and the excited state. When  $\chi_e = \chi_g$  and  $m = 0$ , these integrals have a simple analytical expression,

$$|\langle \chi_{em} | \chi_{gn} \rangle|^2 = e^{-S} \frac{S^n}{n!} \quad (2.3)$$

**Note:** The 1D model works well for  $S \gg 1$ . For  $S < 1$ , there are deviations in the positions of the PSB peaks. However the above discussion provides well, a physical understanding of the Huang-Rhys factor. A simulated spectra for the three cases is presented below, with the blue lines depicting the spectra simulated with the 1D model discussed above.

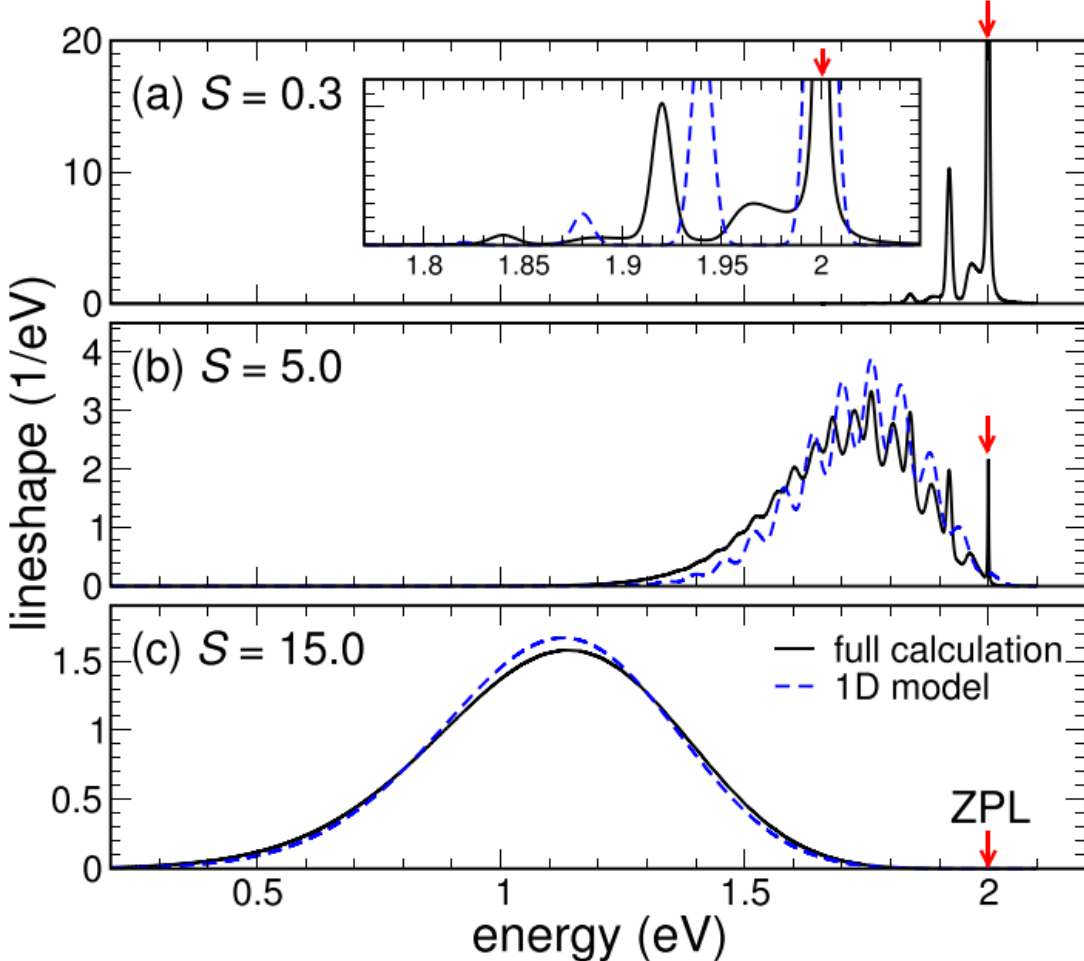


Figure 2.2: Luminescence lineshapes of three model defects. (a) Weak electron-phonon coupling (Huang-Rhys factor  $S = 0.3$ ). (b) Intermediate electron-phonon coupling ( $S = 5.0$ ). (c) Strong electron-phonon coupling ( $S = 15.0$ ). The ZPL is indicated with a (red) arrow. Solid line shows the actual luminescence lineshape, and the dashed line shows a calculation based on a one-dimensional configuration coordinate diagram (“1D model”). A comparison can be made between this figure and Fig.(2.3) where the two cases have  $S \sim 1$  and  $S < 1$  respectively.

**Group-1 and Group-2 SPEs in hBN:** These are defined wrt the Huang-Rhys Factor of the SPE.  $S > 1 \implies \text{Group 1}$ , while  $S < 1 \implies \text{Group 2}$ .

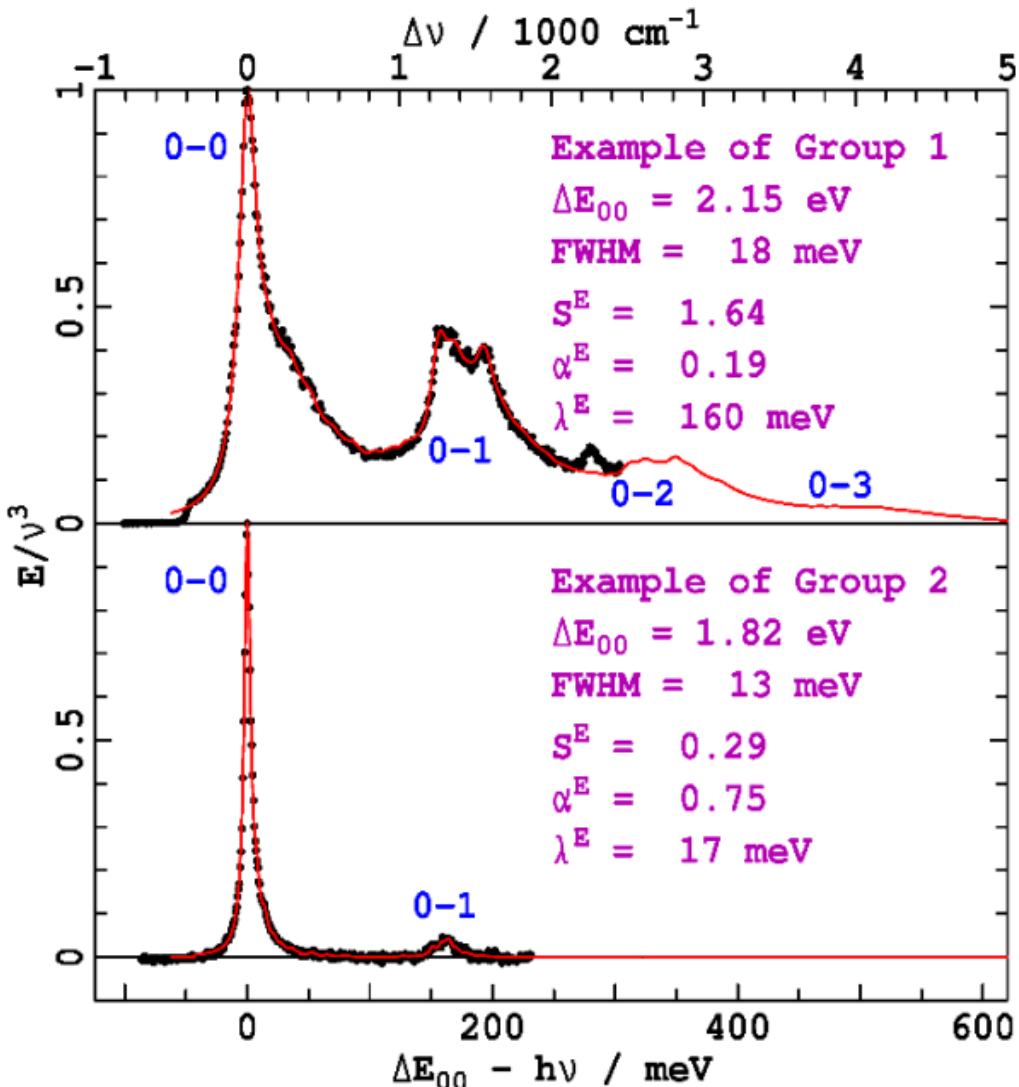


Figure 2.3: Examples of Group-1 and Group-2 visible SPE observed from h-BN defects (black points), and their fits to extrapolated Huang-Rhys models (red lines), using Lorentzian line profiles of specified FWHM. The fits are characterised by their total Huang-Rhys factors, Debye-Waller factors, and reorganization energies, with spectral features labelled as the ZPL (0-0), the primary PSB (0-1), and overtone PSBs (0-2, 0-3, etc.)

## 2.2 Three level model for PL spectra

One method of understanding the PL spectra is through the idea of an asymmetric ZPL with two PSBs red shifted by 165 meV. This redshift corresponds to a well-known phonon mode in hBN. The asymmetry is attributed to phonon interactions. However, when g(2) measurements are performed on these systems, the data could not be well understood by a two-level emission. Other experiments that show this inconsistency are measurements of polarization dependent spectra and time-correlated single photon counting (TCSPC) measurements. The results are best explained via transitions between three defect levels, thus giving rise to two ZPLs, which cause

the asymmetry in the observed ZPL, and corresponding two PSBs. As we will see later, we obtain 4 peaks in the PL spectra of strain activated hBN. From references we find similar peaks present, where the data corresponds to two ZPLs and corresponding two PSBs. We will see how to study the g(2) data in this scenario. Let's discuss the 2-level system model first for g(2):

### Two Level System Model

Consider the two states  $|1\rangle$ , and  $|2\rangle$  as shown in Fig(2.4)(a). We can write the linear rate equations for the occupation of  $|1\rangle$ , and  $|2\rangle$  states as follows:

$$\frac{d}{dt}\rho_1 = -k_{12}\rho_1 + k_{21}\rho_2 \quad (2.4a)$$

$$\frac{d}{dt}\rho_2 = k_{12}\rho_1 - k_{21}\rho_2 \quad (2.4b)$$

Here,  $\rho_1(2)$  is the occupation density at level  $|1(2)\rangle$ , therefore  $\rho_1 + \rho_2 = 1$ .  $k_{12(21)}$  gives the rate of transition of electron from level  $|1(2)\rangle$  to  $|2(1)\rangle$ .  $k_{12}$  is proportional to the excitation power and  $k_{21} = \frac{1}{\tau_2}$ , where  $\tau_2$  is the excited state(2) lifetime. The solution for the two equation (2.4a and 2.4b) comes out to be:

$$\rho_2(t + \tau) = \frac{k_{12}}{k_{12} + k_{21}} \left[ 1 - \exp -\frac{\tau}{\tau_0} \right] + \rho_2(t) \exp -\frac{\tau}{\tau_0} \quad (2.5)$$

where,  $\tau_0 = \frac{1}{k_{12} + k_{21}}$ .

In equilibrium condition,  $(\dot{\rho})_1 = (\dot{\rho})_2 = 0$ ,  $\rho_2 = \frac{k_{12}}{k_{12} + k_{21}}$ .

Take  $\sigma_- = |1\rangle\langle 2|$  and  $\sigma_+ = |2\rangle\langle 1|$ .

To study the  $g^{(2)}$  function, we need to relate the detection of photons at the detectors(annihilation of photon-  $\hat{a}(t, \vec{r})$ ), to the transition operator-  $\sigma_-(t - \frac{|\vec{r} - \vec{r}'|}{c}, \vec{r}')$ . The relationship between the two is linear, therefore:

$$\hat{a}(t, \vec{r}) \propto |1\rangle\langle 2|(t - \frac{|\vec{r} - \vec{r}'|}{c}, \vec{r}')$$

This implies that the detection event of a photon by a detector placed at a position  $\vec{r}$  at time  $t$  is coupled to an atomic transition of an emitter placed at a position  $\vec{r}'$  from state  $|2\rangle$  to  $|1\rangle$  at time  $t|\vec{r} - \vec{r}'|/c$ . Since the expectation value of the photon number operator corresponds to the number of photons in the system, similarly, the expectation value of the operator should correspond to the population of the state  $|2\rangle$ .

Making use of the above discussion  $g^{(2)}(\tau)$  can be written as:

$$g^{(2)}(\tau) = \frac{\langle \hat{E}^{(-)}(t)\hat{E}^{(-)}(t + \tau)\hat{E}^{(+)}(t + \tau)\hat{E}^{(+)}(t) \rangle}{\langle \hat{E}^{(-)}(t)\hat{E}^{(+)}(t) \rangle^2} \quad (2.6)$$

$$= \frac{\langle \hat{a}^\dagger(t)\hat{a}^\dagger(t + \tau)\hat{a}(t + \tau)\hat{a}(t) \rangle}{\langle \hat{a}^\dagger(t)\hat{a}(t) \rangle^2} \quad (2.7)$$

$$= \frac{\langle \hat{\sigma}_+(t)\hat{\sigma}_+(t + \tau)\hat{\sigma}_-(t + \tau)\hat{\sigma}_-(t) \rangle}{\langle \hat{\sigma}_+(t)\hat{\sigma}_-(t) \rangle^2} \quad (2.8)$$

Using the Quantum Regression Theorem, we get:

$$\langle \hat{\sigma}_+(t)\hat{\sigma}_+(t+\tau)\hat{\sigma}_-(t+\tau)\hat{\sigma}_-(t) \rangle = \sum_i \alpha_i(\tau) \left\langle \hat{\sigma}_+(t)\hat{A}_i(t)\hat{\sigma}_-(t) \right\rangle \quad (2.9)$$

where,

$$\hat{A}(t+\tau) = \hat{\sigma}_+(t+\tau)\hat{\sigma}_-(t+\tau) \quad (2.10)$$

which again using QRT, its time evolution can be written as:

$$\langle \hat{A}(t+\tau) \rangle = \sum_i \alpha_i(\tau) \left\langle \hat{A}_i(t) \right\rangle \quad (2.11)$$

Since  $\langle \hat{\sigma}_+(t)\hat{\sigma}_-(t) \rangle$  gives the population of state  $|2\rangle$ , we get from eq(2.5):

$$\langle \hat{\sigma}_+(t+\tau)\hat{\sigma}_-(t+\tau) \rangle = \frac{k_{12}}{k_{12} + k_{21}} \left[ 1 - e^{\frac{-\tau}{\tau_0}} \right] + e^{\frac{-\tau}{\tau_0}} \langle \hat{\sigma}_+(t)\hat{\sigma}_-(t) \rangle. \quad (2.12)$$

On comparing the above equation with the evolution expression for  $\langle \hat{A}(t+\tau) \rangle$ , one can identify

$$\hat{A}_1 = 1, \hat{A}_2 = \hat{\sigma}_+(t)\hat{\sigma}_-(t), \alpha_1 = \frac{k_{12}}{k_{12} + k_{21}} \left( 1 - e^{\frac{-\tau}{\tau_0}} \right)$$

and  $\alpha_2 = e^{\frac{-\tau}{\tau_0}}$  By using these identities, we obtain:

$$\begin{aligned} & \langle \hat{\sigma}_+(t)\hat{\sigma}_+(t+\tau)\hat{\sigma}_-(t+\tau)\hat{\sigma}_-(t) \rangle \\ &= \frac{k_{12}}{k_{12} + k_{21}} \left[ 1 - e^{\frac{-\tau}{\tau_0}} \right] \langle \hat{\sigma}_+(t)\hat{\sigma}_-(t) \rangle \\ &+ e^{\frac{-\tau}{\tau_0}} \langle \hat{\sigma}_+(t)\hat{\sigma}_+(t)\hat{\sigma}_-(t)\hat{\sigma}_-(t) \rangle \end{aligned}$$

As  $\hat{\sigma}_-(t)\hat{\sigma}_-(t)|2\rangle = \hat{\sigma}_-(t)|1\rangle = 0$ , with  $|1\rangle$  being the ground state, then

$$\langle \hat{\sigma}_+(t)\hat{\sigma}_+(t)\hat{\sigma}_-(t)\hat{\sigma}_-(t) \rangle = 0$$

Considering  $\langle \hat{\sigma}_+(t)\hat{\sigma}_+(t) \rangle$  as the population of the state  $|2\rangle$  in equilibrium, i.e.,  $\rho_2(\infty)$ , the second order correlation function for the fluorescence light of a 2-level system is

$$\begin{aligned} g^{(2)}(\tau) &= \frac{\langle \hat{\sigma}_+(t)\hat{\sigma}_+(t+\tau)\hat{\sigma}_-(t+\tau)\hat{\sigma}_-(t) \rangle}{\langle \hat{\sigma}_+(t)\hat{\sigma}_-(t) \rangle^2} = \frac{\rho_2(0+\tau)}{\rho_2(\infty)} \\ &= 1 - e^{\frac{-\tau}{\tau_0}} \end{aligned}$$

at  $\tau = 0, g^{(2)}(\tau) = 0$ . Therefore, a non-resonantly driven 2-level system behaves as an SPS, emitting light in the SP state. The anti-bunching decay time  $\tau_0$  for zero excitation power (i.e.,  $k_{12} = 0$ ) is  $\tau_0(P \rightarrow 0) = 1/k_{12}$ . Since  $k_{12}$  is the decay time of the excited state,  $\tau_0(P \rightarrow 0)$  is the fluorescence lifetime of the 2-level emitter.

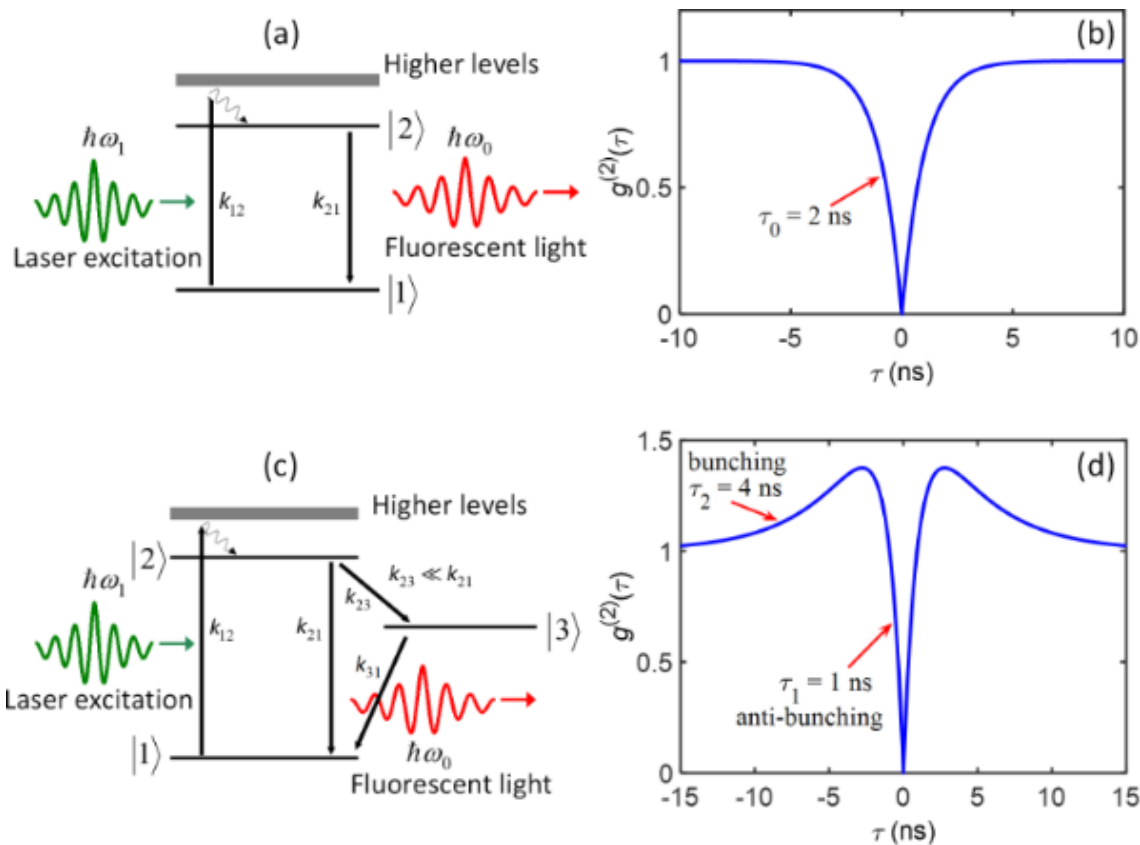


Figure 2.4: (a) Schematic representation of spontaneous emission from a non-resonantly driven 2-level system. (b) The second order correlation function for a 2-level system,  $g^{(2)}(\tau)$ . (c) Schematic representation of spontaneous emission from a non-resonantly driven 3-level system. (d) The second order correlation function for a 3-level system.

### Three level system model

A 3-level system comprises an intermediate meta-stable state along with the ground and the excited states. Fig. (2.4 (c)) shows the representation of a 3-level system. The state  $|3\rangle$  is a metastable state, i.e., transitions between it and the ground state  $|1\rangle$  will occur at a much longer time scale compared to transitions between the excited state  $|2\rangle$  and the ground state  $|1\rangle$ . The system non-radiatively relaxes between the excited triplet state  $|2\rangle$  and the singlet meta-stable state  $|3\rangle$ . These non-radiative relaxation processes between the different spin states are known as inter-system crossing (ISC). The decay process between the different spin states occurs at a much slower rate and is mediated by the spin-orbit coupling. Therefore,  $k_{23} \ll k_{21}$ . This results in the metastable nature of the state  $|3\rangle$ . From the metastable state  $|3\rangle$ , the system finally relaxes to the ground state via phosphorescence. Fluorescence occurs when the system relaxes from state  $v|2\rangle$  to state  $v|1\rangle$  via spontaneous emission, emitting a photon of energy  $\hbar\omega_0$ . In the same approximation as the 2-level systems, the rate equations for the 3-level system are:

$$\begin{aligned}\dot{\rho}_1 &= -k_{12}\rho_1 + k_{21}\rho_2 + k_{31}\rho_3, \\ \dot{\rho}_2 &= k_{12}\rho_1 - (k_{21} + k_{23})\rho_2, \\ \dot{\rho}_3 &= k_{23}\rho_2 - k_{31}\rho_3,\end{aligned}$$

The second order autocorrelation function for the three-level system is given by:

$$g^{(2)}(\tau) = 1 - (1 + c)e^{\frac{-\tau}{\tau_1}} + ce^{\frac{-\tau}{\tau_2}}$$

Here the decay times  $\tau_1, \tau_2$  and the coefficient  $c$  are given by

$$\frac{1}{\tau_1} = k_{12} + k_{21}, \frac{1}{\tau_2} = k_{31} + \frac{k_{23}k_{12}}{k_{12} + k_{21}}, c = \frac{k_{12}k_{23}}{k_{31}(k_{12} + k_{21})}.$$

In the above  $g^{(2)}(\tau)$  function,  $\tau_1$  represents the anti-bunching decay time and  $\tau_2$  represents the bunching process (Figure 1d). This is because the rates  $k_{23}$  and  $k_{31}$  are much smaller compared to  $k_{21}, \tau_1 \ll \tau_2$ . This means that the antibunching process occurs at a much faster time scale compared to the bunching process.

#### 2.2.1 How does strain help?

The idea of the project is to produce single photon emitters at specific positions, thus, deterministic. We claim that this is achieved by the nanopillar array, since they produce strain in the hBN crystal. In the approximation of thin - plate theory, we can say that the strain is in plane. This strain causes a change in the lattice constants and the tight-binding parameters of the hBN lattice. Thus a change in the conduction band and valence band profile. This change can be quantified by the use of the Föppl-von Kármán equations[13]:

$$D\Delta^2\zeta = P \tag{2.13}$$

Here,  $P$  is the pressure the atomic layer experiences,  $\zeta$  is the height profile of the atomic layer, and  $D$  is the flexural rigidity of the TMD layer defined as:

$$D = \frac{Eh^3}{12(1 - \sigma^2)} \tag{2.14}$$

Eq(2.13) can be solved with an appropriate pressure function, here we consider 3 pressure models[ [\[14\]](#)]:

Model	$P$
Zero Pressure	0
Constant Pressure ( $P_c$ )	$\frac{64DH}{r_T^4}$
van der Waals Pressure ( $P_{vdW}$ )	$\frac{\mathcal{H}_{TMD-Sub}}{(h/2+\zeta)^3}$

Table 2.1: Pressure Models

Eq(2.13) is solved in Mathematica for the three pressure models, since analytical solution is not possible for  $P_{vdW}$  model. The notebooks used can be found [here](#).

$$\mathbf{P} = \mathbf{0}$$

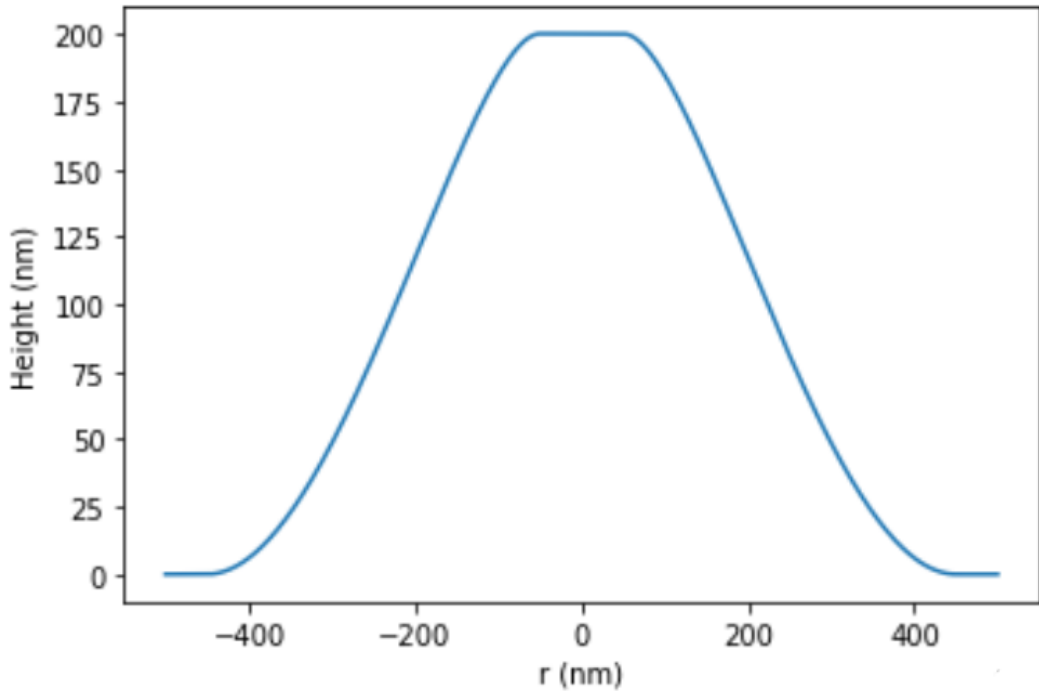
We solve the following equation:

$$D\Delta^2\zeta(\rho) = 0 \quad (2.15)$$

for the boundary conditions:

$$\begin{aligned} \zeta(r) &= H \\ \zeta(r_T) &= 0 \\ \zeta'(r) &= 0 \\ \zeta'(r_T) &= 0 \end{aligned} \quad (2.16)$$

We plot the height profile v/s the radial coordinate  $\rho$  for  $r = 200\text{ nm}$ ,  $H = 200\text{ nm}$  and  $r_T = 450\text{ nm}$ .

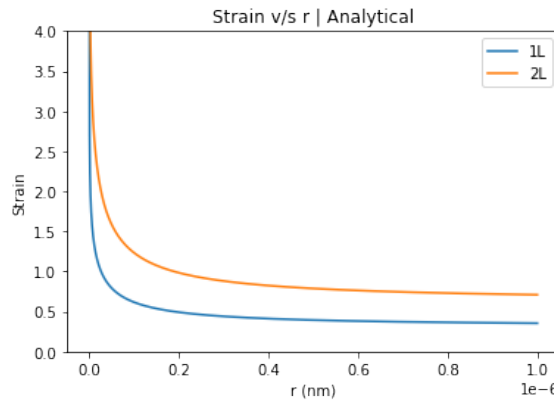

 Figure 2.5:  $P=0$  Height Profile

The height profile can be used to find the strain profile for various radii of nanopillar, and also the conduction band potential minimum ( $V_{cb}$ ), calculated for the K(K') point of the Brillouin zone.

The relation between tensile strain maximum and the nano-pillar radius is given by[[13]]:

$$\mathcal{T} = Tr[\epsilon_{ij}] = \frac{(2\sigma - 1)h}{1 - \sigma} \Delta\zeta \quad (2.17)$$

Here, the Laplacian is wrt.  $\rho$ , but we plot strain v/s the nano-pillar radius( $r$ ).



(a) Calculated

Figure 2.6: Uniaxial tensile strain values as a function of the nano-pillar radius, calculated at the topmost edge of the nano-antenna ( $H = 200$  nm) for both single and double layer WSe<sub>2</sub>.

From the uniaxial strain we calculate the conduction band potential  $V_{cb}$  using the following relation[[13]]:

$$V = \begin{pmatrix} V_{vb} & 0 \\ 0 & V_{cb} \end{pmatrix} = \begin{pmatrix} \delta_v \mathcal{T} & 0 \\ 0 & \delta_c \mathcal{T} \end{pmatrix} \quad (2.18)$$

where  $\delta_v$  and  $\delta_c$  are the parameters governing the strain response for the conduction ( $V_{cb}$ ) and valence band ( $V_{vb}$ ) at the K(K') point, respectively. Using this relation, provides the Poisson's equation for the conduction band and valence band potentials from Eq(2.13). Figure (2.7) shows the conduction band potential as a function of the radial coordinate for  $P = 0$ .

## Height Profile and Conduction Band Potential

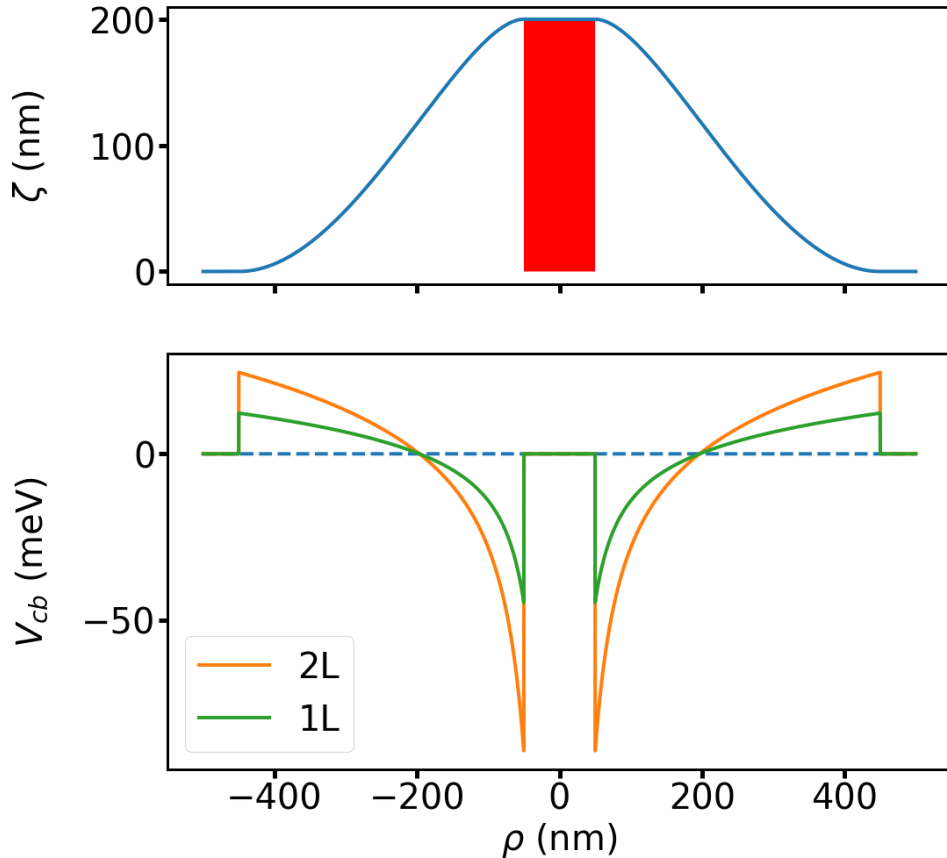


Figure 2.7: Conduction band potential minimum ( $V_{cb}$ ), calculated for the K(K') point of the Brillouin zone, for both single (1L) and double (2L) layer WSe2, relative to the height profile shown in Fig. (2.5)

$$\mathbf{P} = \mathbf{P}_c$$

We solve the following equation[ [14]]:

$$D\Delta^2\zeta(\rho) = \frac{64DH}{r_T^4} \quad (2.19)$$

for the boundary conditions Eq.(2.16). Consider the relation:

$$\beta = \frac{H}{r_T^4} \quad (2.20)$$

Thus,  $P_c$  can be written as:

$$P_c = 64DH\beta \quad (2.21)$$

So, there are two possibilities to vary the pressure  $P_c$ . Either we vary  $r_T$  or  $\beta$ . Let us plot the height profile for both the cases.

$$\mathbf{P} = \mathbf{P}_{vdW}$$

We solve the following equation[ [14]]:

$$D\Delta^2\zeta(\rho) = \frac{\mathcal{H}_{TMD-Sub}}{(h/2 + \zeta)^3} \quad (2.22)$$

for the boundary conditions Eq.(2.16).

$$\Delta^2\zeta(\rho) = \frac{\mathcal{H}_{TMD-Sub}}{D} \frac{1}{(h/2 + \zeta)^3} \quad (2.23)$$

Since we did not have a reliable source for the Hamaker constant value, we will vary the value of the factor  $H/D = \frac{\mathcal{H}_{TMD-Sub}}{D}$  and see if the results match the reference plots[[14]].

For  $H/D = 1/10$ , the plots are similar, thus we are able to achieve the required qualitative behaviour of the height profile in van der Waals pressure model.

### Strain v/s Nanopillar radius

After comparing the height profiles for various pressure models, we work towards the strain profile for varying nanopillar radius. To do so, we use Eq(2.17).

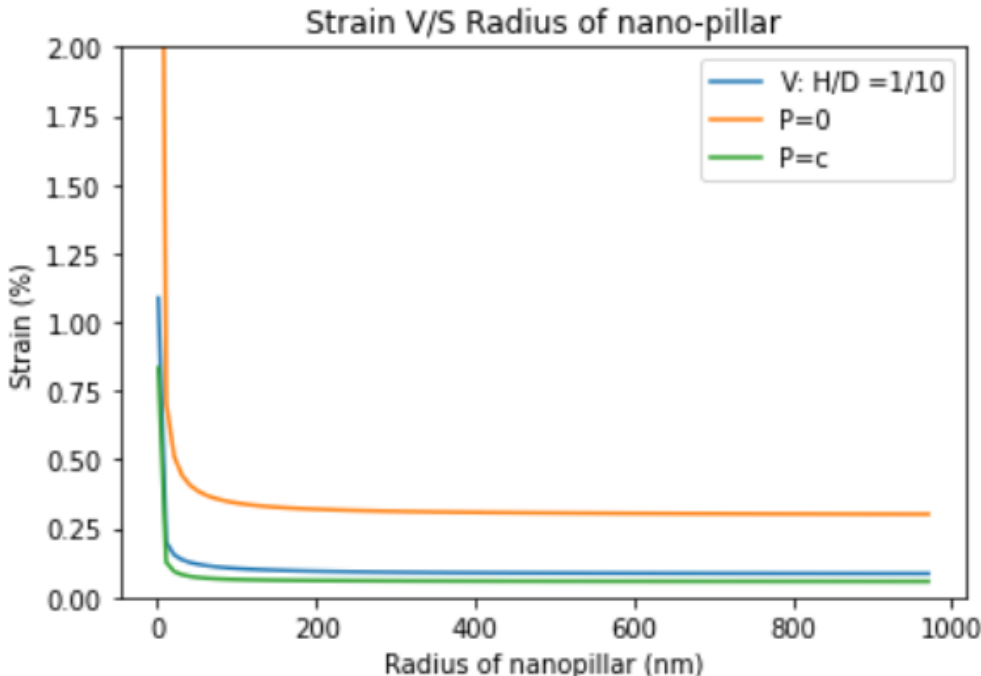


Figure 2.8: Strain v/s nano-pillar radius for the three pressure models

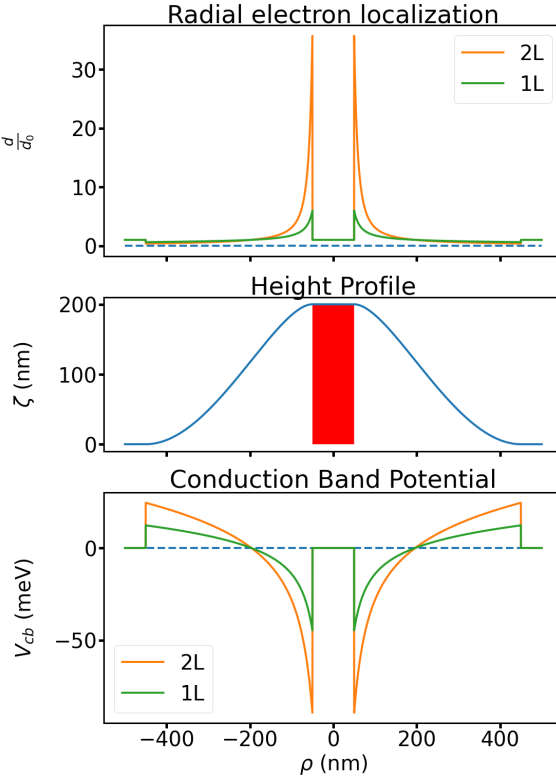


Figure 2.9: Radial charge localisation around the nanopillar geometry plotted alongside the nanopillar geometry and the conduction band profile.

## Charge Trapping

The effect of the change in the band potential is that it creates a trap for electrons/holes to settle into, thus increasing the local concentration of charge. This change in local charge concentration can be modelled from the deformation potential simulated above.

$$V_{DP}(\rho) = \alpha \Delta \zeta(\rho) \quad (2.24)$$

The deformation potential is proportional to  $\Delta \zeta(\rho)$ , where  $\alpha$  is different for holes and electrons. Holes are described by the deformation potential amplitude at the valence band maximum  $\alpha_{VBM} \sim 1.64\text{eV}$ , and electrons are described by the deformation potential amplitude at the conduction band minimum  $\alpha_{CBM} \sim 4.67\text{eV}$ . These parameters are for the K-point of hBN. The deformation potential at the top layer of the flake and each charge carrier is depicted in Fig. (2.7). Each estimated potential is sufficient to localize electrons or holes at the lip of the pillar and vice-versa at the base.

$V_D$  depends on  $T_z$  linearly, and is zero along the mid plane, so it reaches its maxima or minima in  $z$  on the top and bottom surfaces of the flake. That is, where there is tensile strain on the top surface there is compressive strain on the bottom surface, and vice versa. Boltzmann statistics are used to estimate the charge density confined by the deformation potential. The Boltzmann equation,  $d(r, z) = d_0 e^{-V_{DP}(r, z)/kT}$ , describes the local density of carriers and is depicted in Fig. (2.9), where  $d_0$  is the density in the absence of deformation.

# Chapter 3

## Experiments

### 3.1 Sample Preparation

To be able to induce strain in hBN samples with the help of nanostructured pillars, we require thin layers of hBN. To this end we tried to achieve monolayers by implementing Nitto blue tape exfoliation.

#### 3.1.1 Nitto Blue tape exfoliation

##### Procedure:

- Take a few crystals of the van der Waals material on a piece of Nitto blue tape.
- Stick another piece of the tape on the first one and peel. This would transfer some of the crystal on the second tape.
- Keep the first tape as the parent tape to use for exfoliation with other tape pieces.
- Fold the second tape in half, and perform peeling and sticking action on the fold for about a 10 times to achieve possible monolayer.
- Transfer the monolayer on the choice substrate to examine the achieved exfoliated material. We used PDMS for ease of further transfer.

We obtained multiple monolayer hBN samples between  $10\mu m$  and  $20\mu m$  in width.

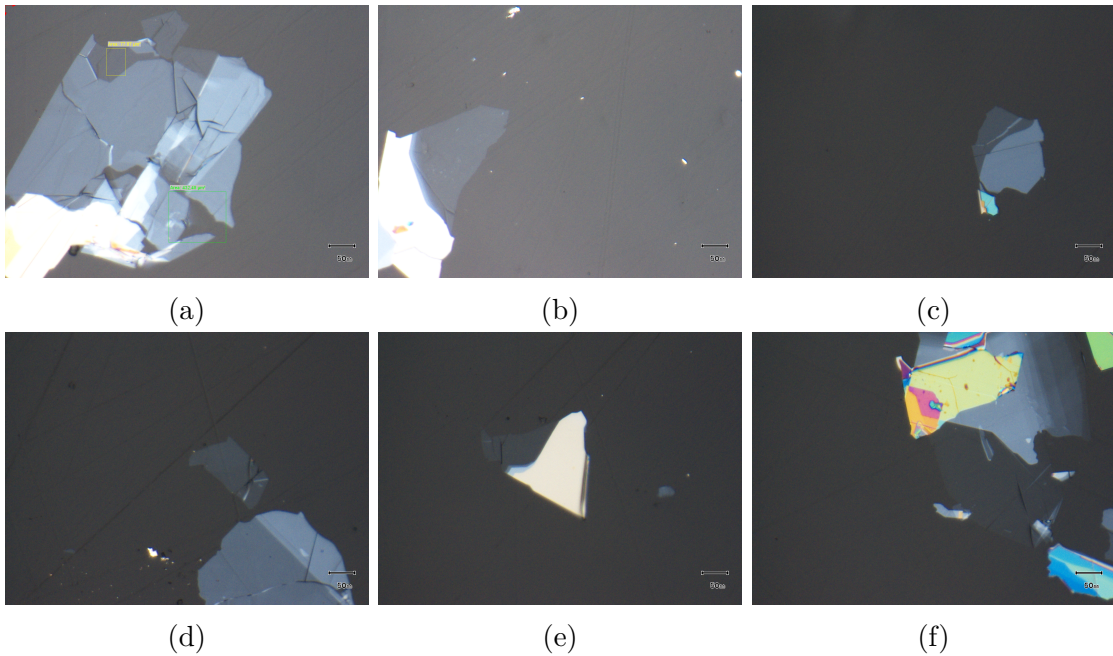


Figure 3.1: Nitto Blue Tape Exfoliation : Exfoliated Samples. Almost no tape residue on the PDMS substrate and hBN samples. Flake sizes are much larger than  $10\mu m$ . The monolayers obtained lie in the size range of  $10\mu m - 20\mu m$  in diameter

## 3.2 Sample Characterisation

Photoluminescence and Raman Spectroscopy was performed on the 2D hBN samples obtained on PDMS. Combined Raman and PL spectra of a few samples is presented below.

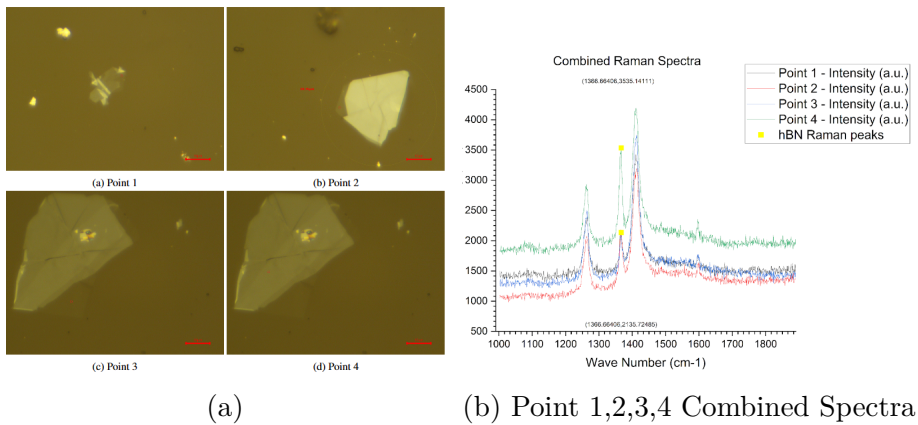


Figure 3.2: (a) Positions where the Raman spectra was taken. (b) Corresponding Raman spectra, showing the effect of change of layer count on the Raman spectra, clearly indication the hBN Raman peak  $\sim 1365cm^{-1}$ , along width a PDMS peak.

## 3.3 hBN Transfer on Gold Nanocones

A periodic lattice of Gold nanocones lithographed on Si-SiO<sub>2</sub> substrate with electron beam lithography was used as the substrate for the transfer of few layer hBN de-

veloped through tape exfoliation. Gold nanocones of various periodicity and radius were used. An SEM image marking the specifications is presented below.

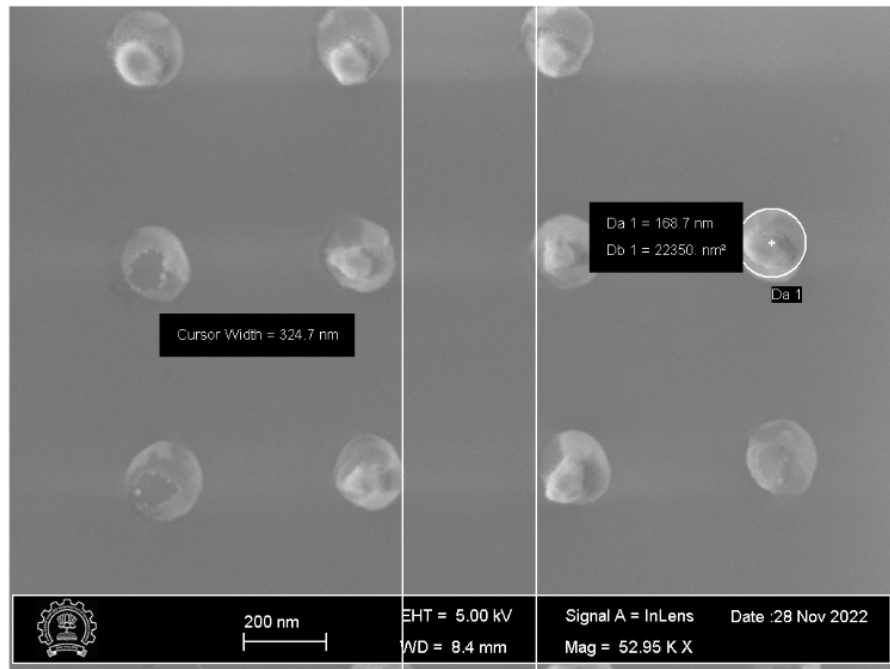


Figure 3.3: The lithographed gold nanocones [height  $\sim 100\text{nm}$ ] on  $\text{SiO}_2$ [ $\sim 300\text{nm}$ ] on a Si substrate, with the diameter and periodicity marked.

The structure of the cones is presented below:

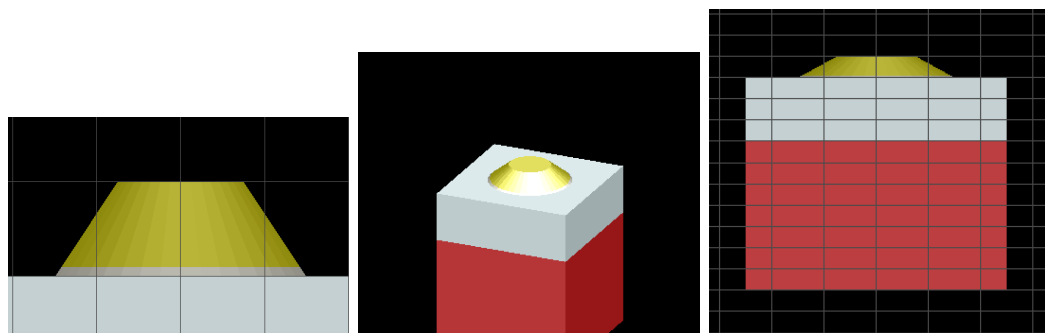


Figure 3.4: Simulation of the geometry of a single nanocone

The prepared hBN samples on PDMS were transferred on the nanocones via a dry transfer method. Following are the obtained transferred smamples. There are some considerations while transferring the sample.

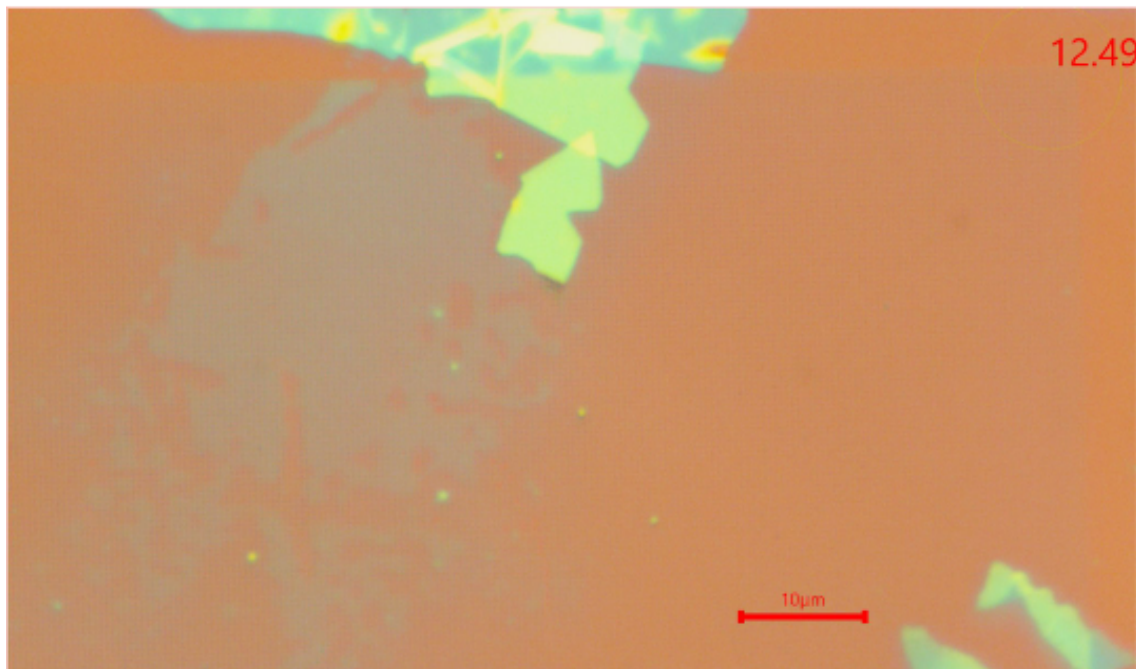


Figure 3.5: A transferred hBN sample on the periodic nanocone structure. Residue due to PDMS is visible on the nanocones.

Once the sample is created, a sequence of experiments are performed to ascertain their properties.

**Raman Spectroscopy** Although the transferred hBN is visible at 100x magnification, a further test would be to perform Raman spectroscopy to obtain the hBN peak  $\sim 1365\text{cm}^{-1}$ . We performed this on the sample shown below.

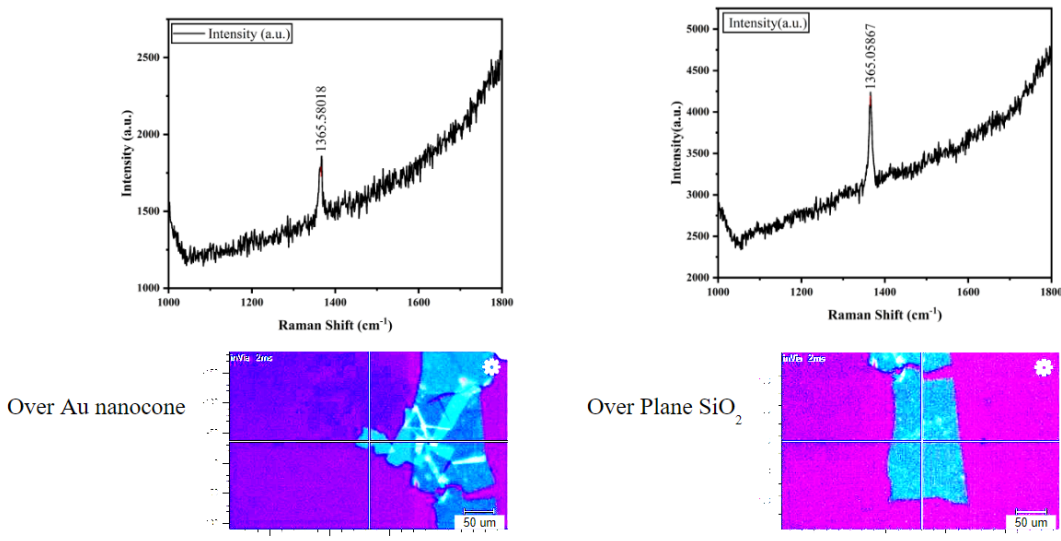


Figure 3.6: The clear peaks at  $\sim 1365\text{cm}^{-1}$  indicates the success of the transfer process

Once the hBN is transferred. since the process is a dry transfer method, where we

basically stamp the hBN on the nanocone pattern, we can not be sure of the topography of the hBN surface, whether the hBN has assumed the pattern topography well or not. To further establish it, we can perform treatment with ethylene glycol, which upon drying would force the hBN to assume the structure of the cones, or tent according the the spacing between cones, and their height profiles. However, we haven't performed such a treatment on any sample.

**Atomic Force Microscopy** To study the surface topography, we performed Atomic Force Microscopy. The results are presented below.

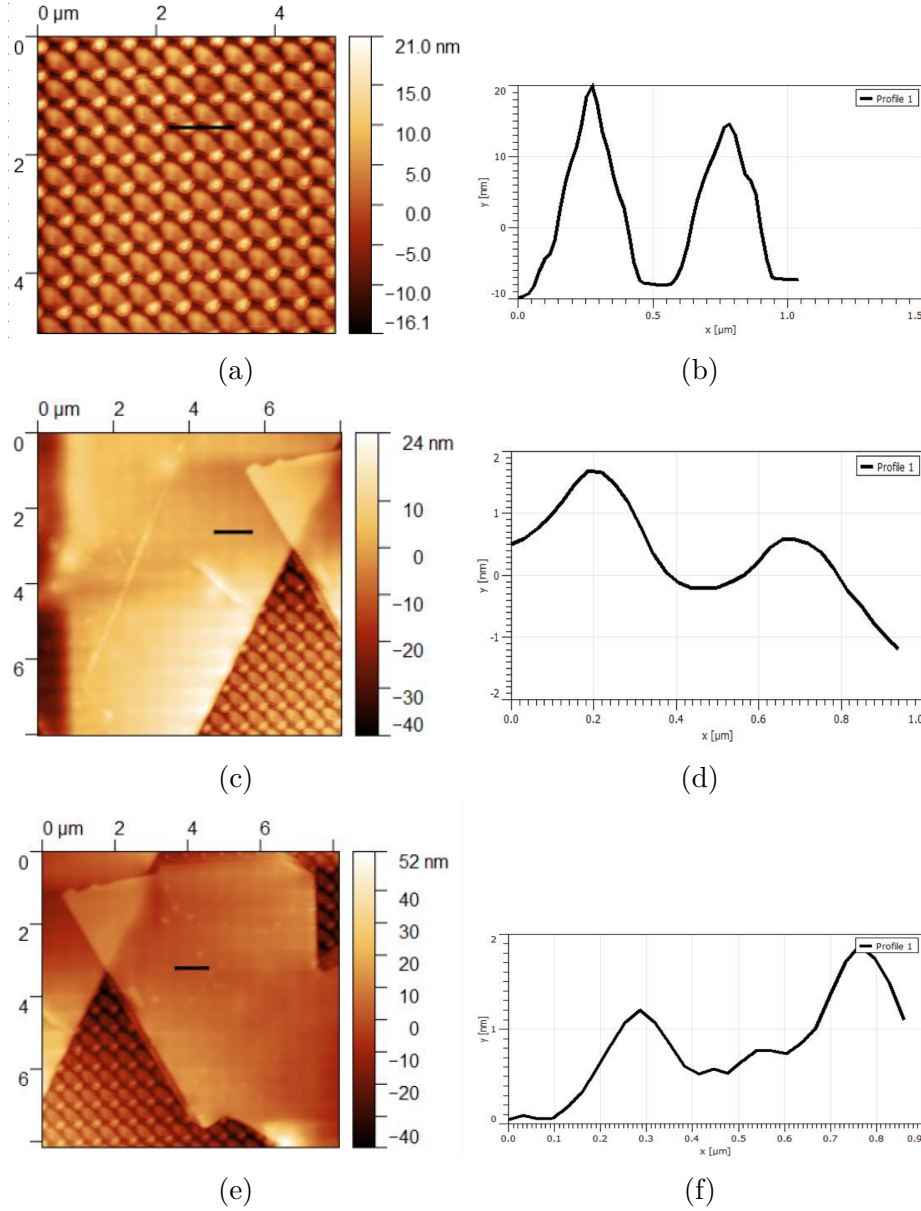
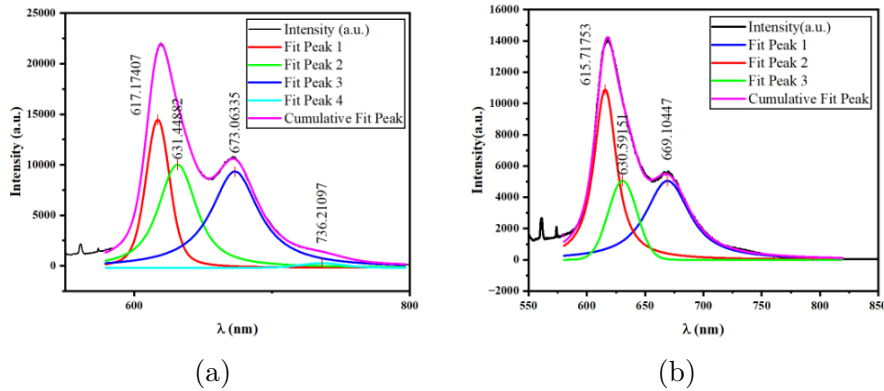


Figure 3.7

There are issues in the obtained surface topography. In **Fig. (a)**, we see a periodic pattern, but there are two sub patterns, first, smaller circles, which are  $\sim 15\text{nm}$  height, and second, larger circles which are at around 5 to 10 nm. Since such a pattern is not visible in the SEM images, we assume that this is a tip artefact,

however, even after changing the tip, we found similar issues and, thus we assume an issue with the facility at the time of the experiment. However, since the use of AFM for us was to ascertain that hBN has assumed the surface topography of the cone pattern, we get satisfactory results from the data, as shown in **Fig. (d)**. The change in the height of the peaks in **Fig. (d)** is attributed to the non-zero angle at which the tip is traversing the surface of the sample, as the sample is not flat from the bottom.

Once these two points were confirmed, we obtained the PL spectrum of the two points in Fig. (3.6).



**Photoluminescence Spectroscopy** We deconvolved the PL spectrum with Gaussian peaks, and obtain three major peaks and one minor peak at  $\sim 736\text{nm}$ . The three peaks are present in both hBN positions, with and without nanocones, however, the plasmonic enhancement of emitted intensity is clear in the Fig. (3.8a) (maximum intensity  $\sim 22500$ ) as compared to Fig. (3.8b) (maximum intensity  $\sim 14000$ ).

We wish to study the effect of the plasmonic nanocone pattern of particular dimensions on the SPEs in hBN ranging from monolayer to multilayer. So we transferred a hBN sample with multi and mono layers on a gold nanocone pattern of dimensions as shown in Fig. (3.3). The sample is shown below:

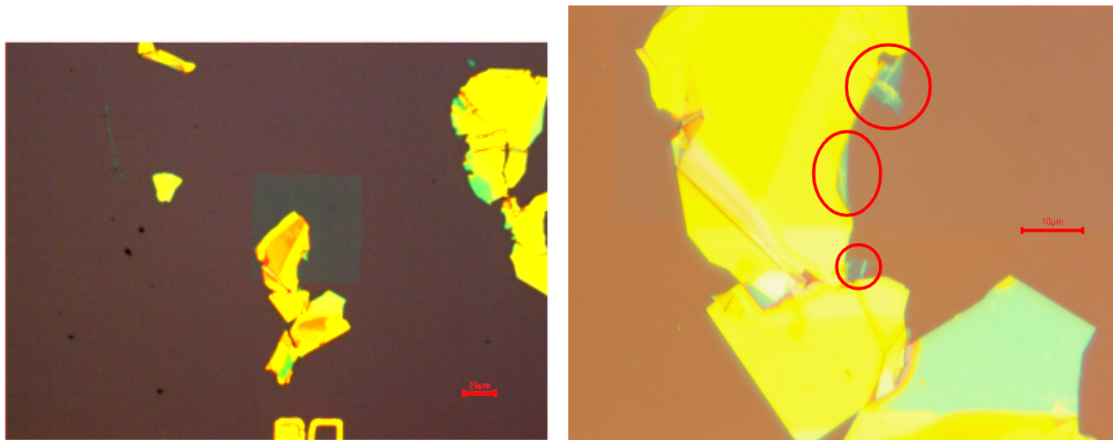
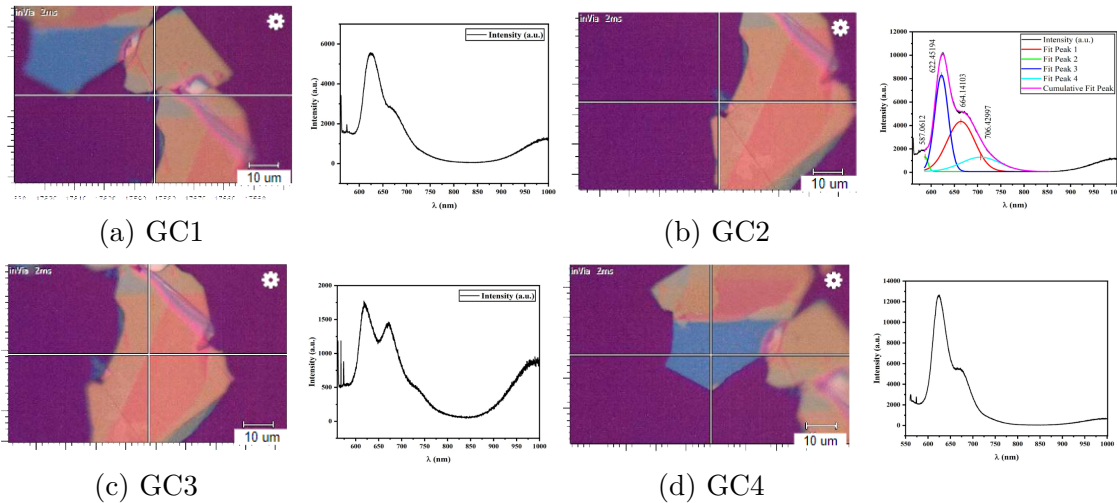


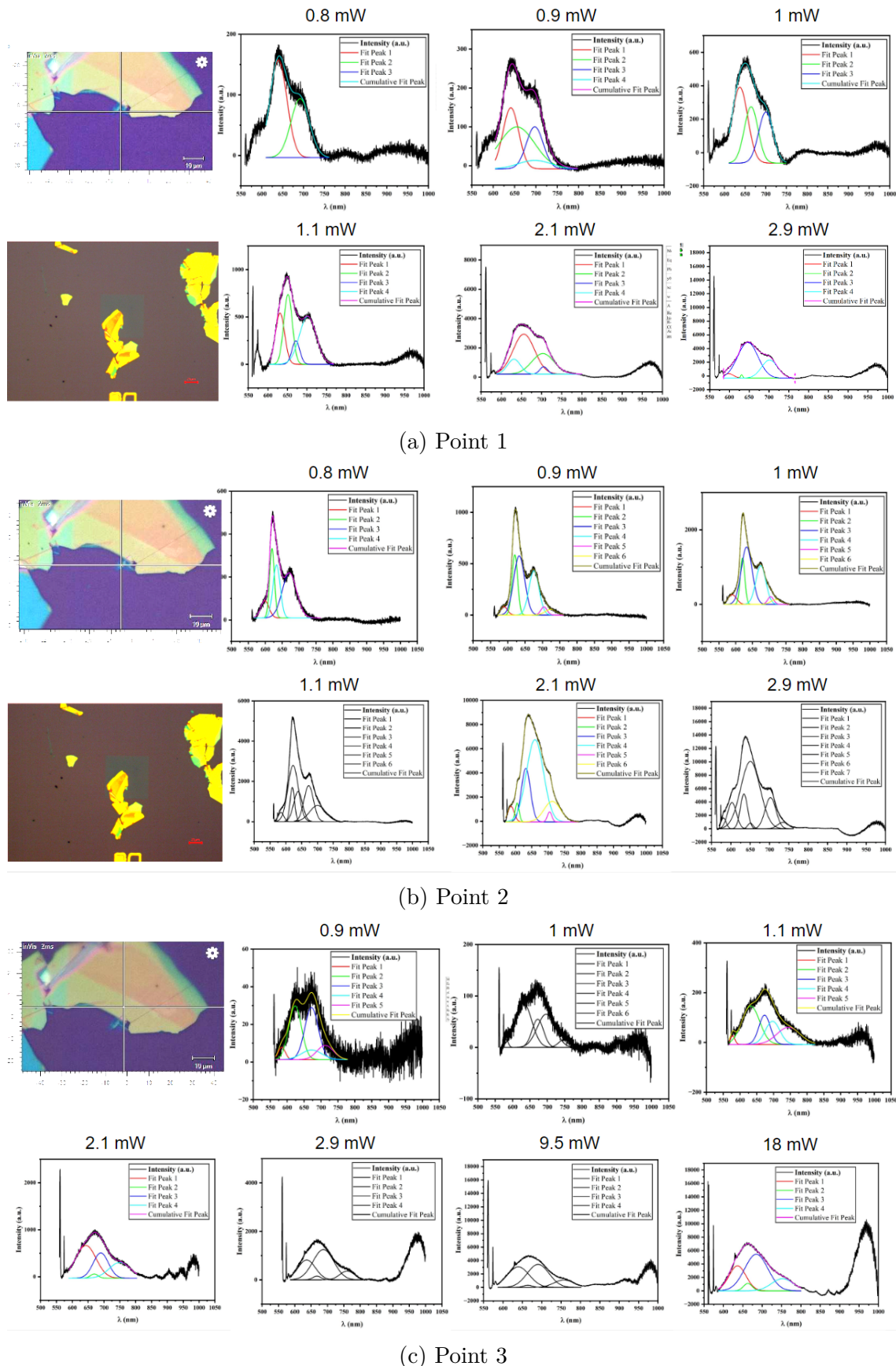
Figure 3.9: Caption

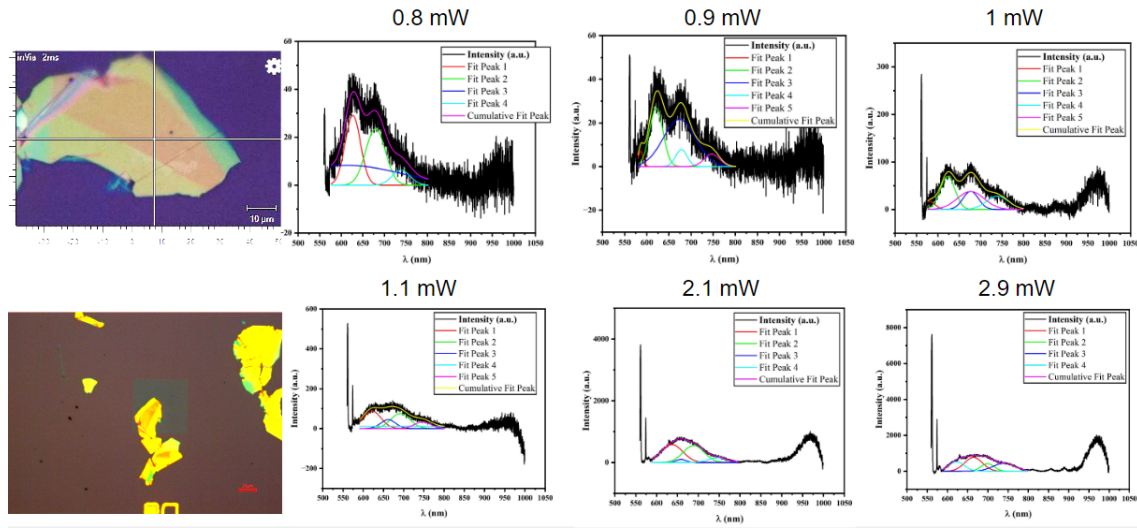
We performed PL spectroscopy at the following 4 points for preliminary study. The results were promising with PL peaks appearing at similar wavelengths. The lower peak intensities point to the possibility of SPEs being the reason for these emissions.



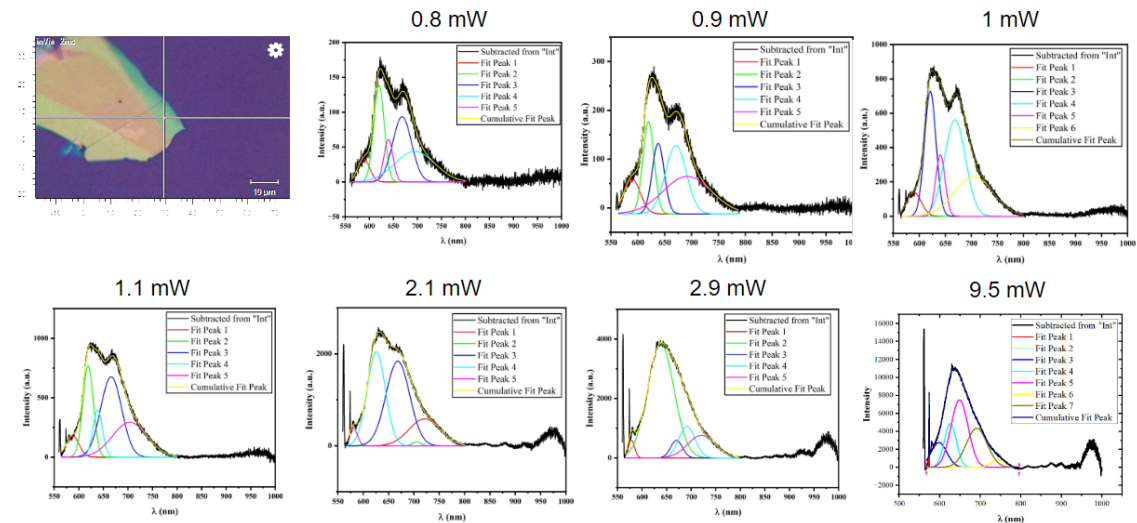
### Power Dependent PL

To understand saturation effects in PL emission and the corresponding intensities, we performed a power dependent spectroscopy. The corresponding PL plots are presented below:



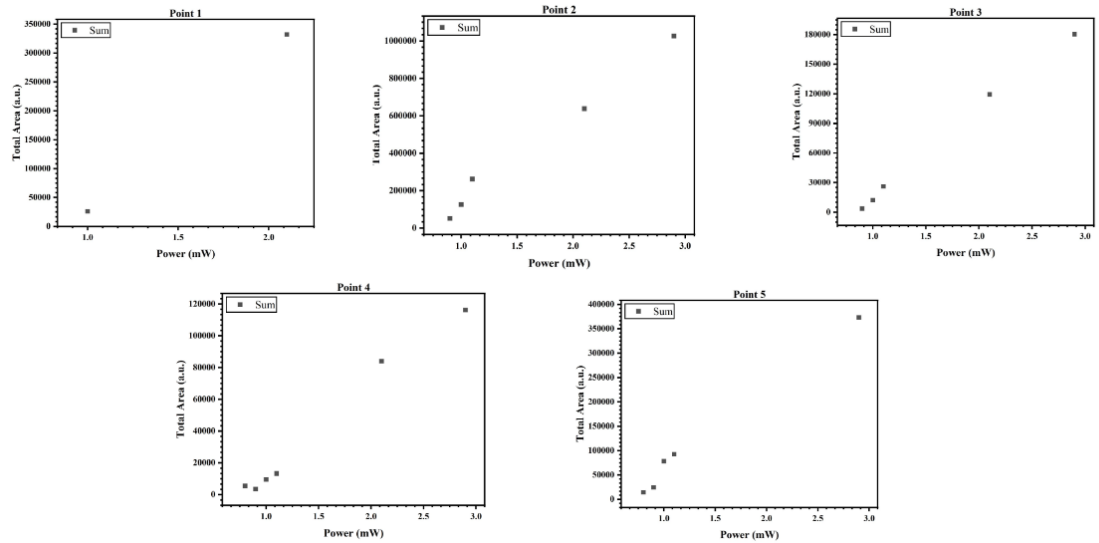


(d) Point 4

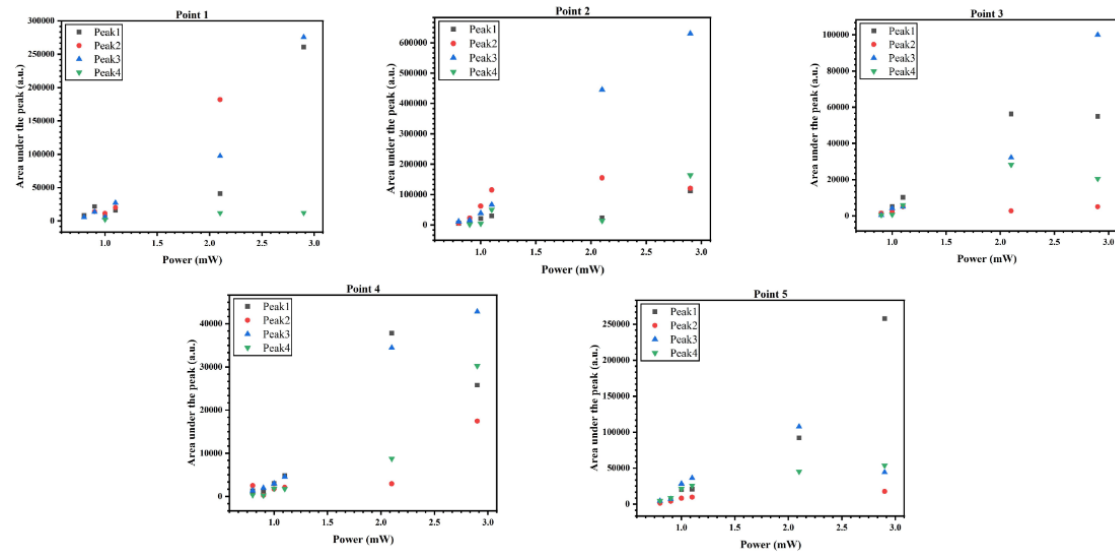


(e) Point 5

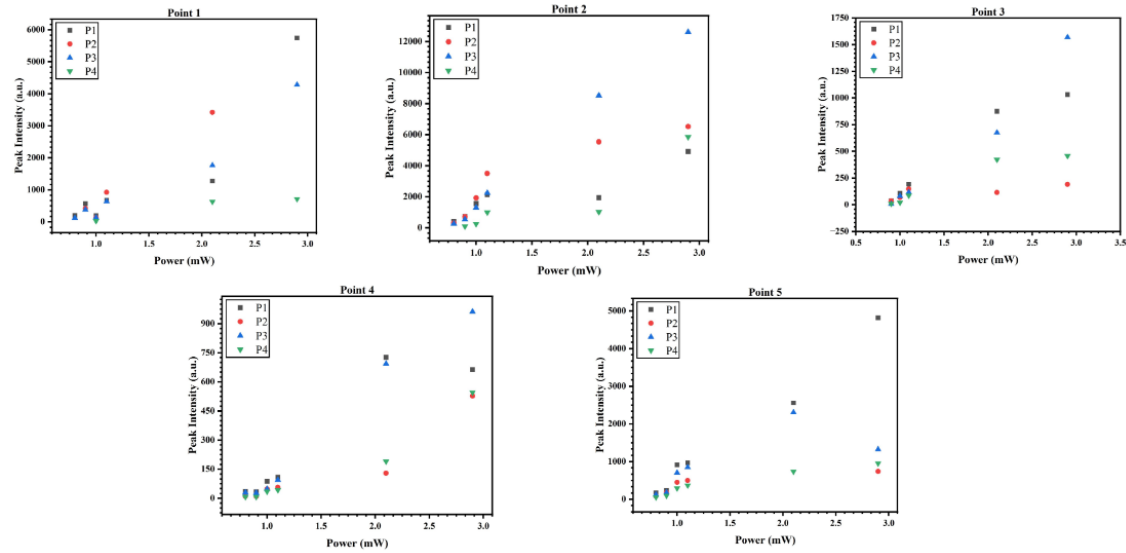
The total emission, the emission per peak, and the peak intensities are plotted wrt incident power.



(a) Total emission v/s Incident Power



(b) Emission per peak v/s Incident Power



(c) Emission Intensity per peak v/s Incident Power

# Chapter 4

## Lumerical Simulations

### 4.1 Surface Plasmon Resonance

Surface plasmons are coupled oscillations that arise from the interaction between light and the conduction electrons in a metal or semiconductor. The interaction can occur on a scale much smaller than the wavelength of light, effectively squeezing light into tiny, sub-wavelength volumes. Within these volumes, the optical fields can be strongly enhanced, beyond that of the incident wave used to create the excitation. By leveraging surface enhancement, it is possible to increase the functionality and performance of optical materials.

The surface plasmon is an excitation that travels along the interface between a conducting material and air. Bound to the surface of the conductor, the surface plasmon is an example of a surface mode, which does not radiate into space. We can characterize a surface plasmon by its spatial wavelength along the surface and its frequency of excitation. The dispersion relation can be found as

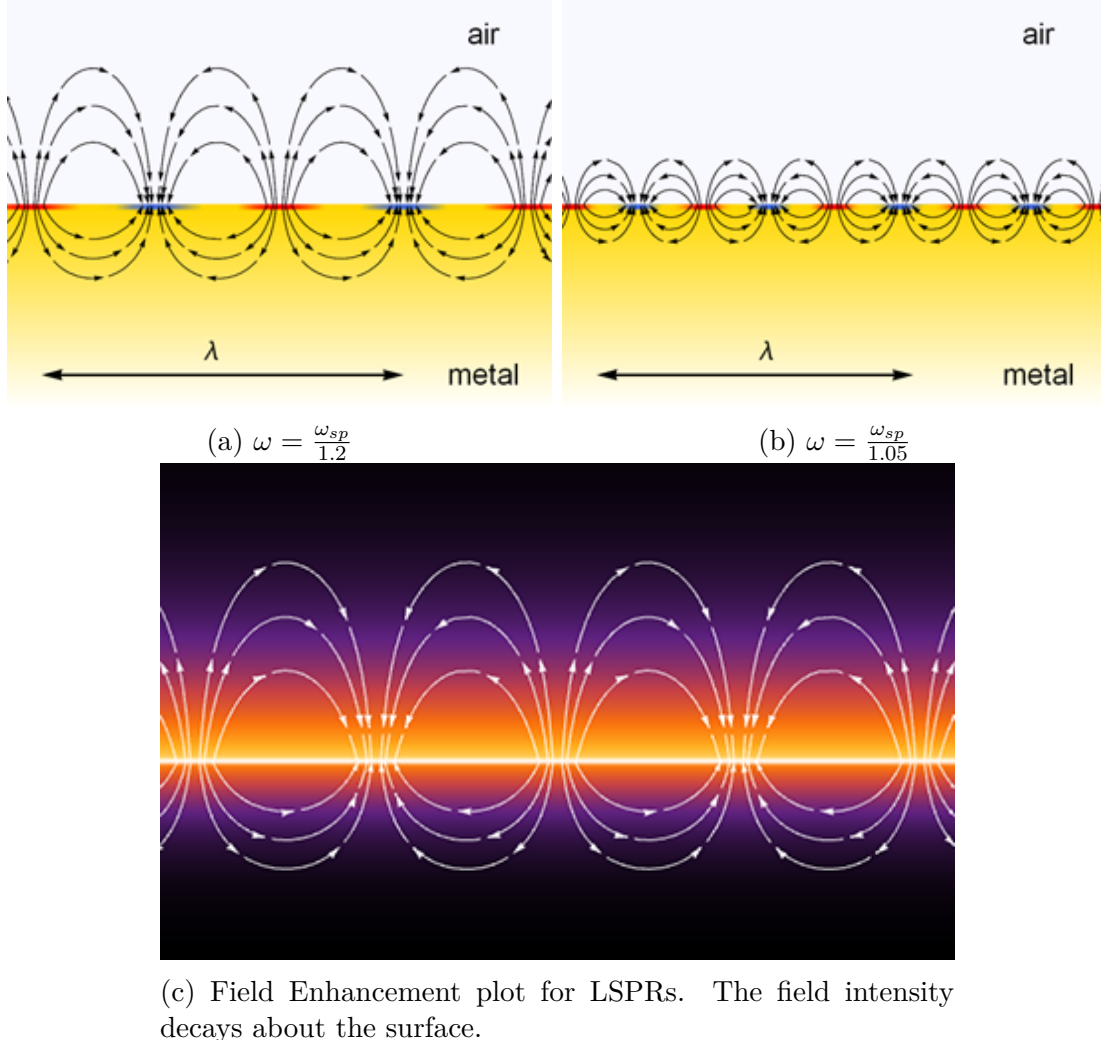
$$k_x = k_0 \sqrt{\frac{\epsilon_0 \epsilon_m(\omega)}{\epsilon_0 + \epsilon_m(\omega)}} \quad (4.1)$$

, where  $k_0$  is the free space wave number,  $\epsilon_0$  is the permittivity of free space, and  $\epsilon_m$  is the frequency-dependent permittivity of the metal or conductor.

The dielectric function of many conductors (such as silver or gold) has the form  $\epsilon(\omega) = 1 - \frac{\omega_p^2}{\omega^2}$ , where material absorption has been ignored, and the values are always real. Below the plasma frequency  $\omega_p$ , the values of the dielectric function are negative. From the surface plasmon dispersion relation, it can be seen that solutions exist for  $\epsilon(\omega) < 1$ . The negative dielectric function is what leads to the potential for surface modes, and the reason that metals and other conductors are often referred to as plasmonic materials.

It is possible to visualize the fields of a surface plasmon using the simple form of the dielectric function above. Two possible surface plasmons are shown, one at the frequency  $\omega = \frac{\omega_{sp}}{1.2}$  and the other at the frequency  $\omega = \frac{\omega_{sp}}{1.05}$ . At the former frequency, the fields extend into the air region a bit more, and the surface plasmon wavelength is closer to the free space wavelength. At the latter frequency, which is closer to the

surface plasmon frequency  $\omega_{sp}$ , the fields are more tightly bound to the surface, with the surface plasmon wavelength significantly smaller than the free space wavelength.



(c) Field Enhancement plot for LSPRs. The field intensity decays about the surface.

Figure 4.1: Caption

### Field enhancement and LSPRS

Different geometries of metals, such as nanostructures, support surface plasmons while simultaneously coupling to the radiative field. When the optical fields present on such structures are induced by an incident wave, one can describe the field enhancement as the ratio of the local electric field to that of the incident electric field  $E_{enhance} = \frac{|\vec{E}_{np}|}{|\vec{E}_{inc}|}$ . This field enhancement effect has profound implications for many optical phenomena.

When light interacts with a particle having a dimension much smaller than the wavelength of the light, the particle is polarized, with an induced charge distribution appearing. This polarization can lead to the excitation of localized surface plasmons, which are resonant excitations that are spatially confined to the nanoparticle. Such nanoparticles have unique optical properties that arise from their size and shape, as well as the composition of the nanoparticle and the surrounding medium.

## Coupled LSPRs

The charge distribution on the surface of the nanosphere is limited by dipolar excitation, which leads to only a fairly smooth variation of the charge density. This limits the strength of the fields that can be bound to the surface of the nanoparticle. However, even with this limitation, plasmonic nanospheres are still one of the strongest scattering objects in optics and are widely used in microscopy.

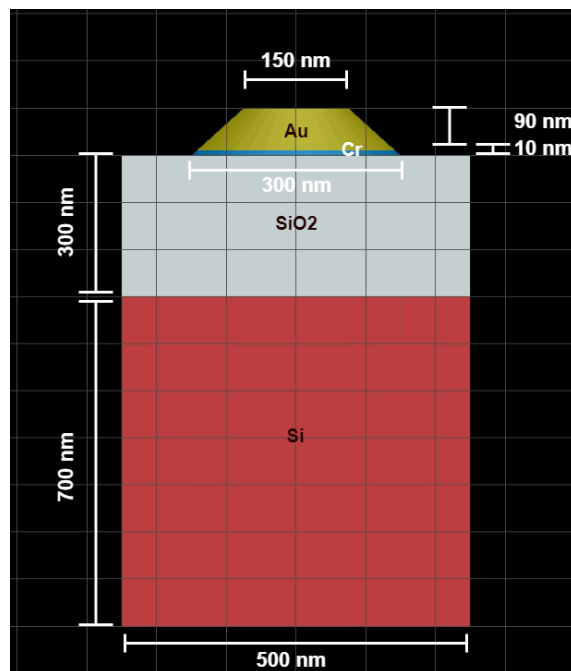
There are higher order modes of surface plasmon resonance that can exist on the nanosphere, but these modes occur at different frequencies and do not inherently couple to an incident plane wave or electrostatic field. This means that if they could be excited, all of the energy would just be lost to resistive currents in the nanosphere.

To unlock these higher order modes, the symmetry of the sphere geometry must be broken. One way to do this is by using two coupled nanospheres separated by a nanometer-scale gap. This causes all of the modes of the individual spheres to couple together, resulting in a tightly localized region between the spheres where the charge density can be extremely large.

In plasmon resonant nanoparticles, the optical fields are enhanced due to the strong coupling between the surface plasmon of the nanoparticle

## 4.2 Periodic array of nanocones - no hBN

To study the field enhancement observed due to the gold nanocones, we performed Finite Domain Time Difference(FDTD) simulations for the nanocone structure in Ansys Lumerical. The structure simulated is presented below.



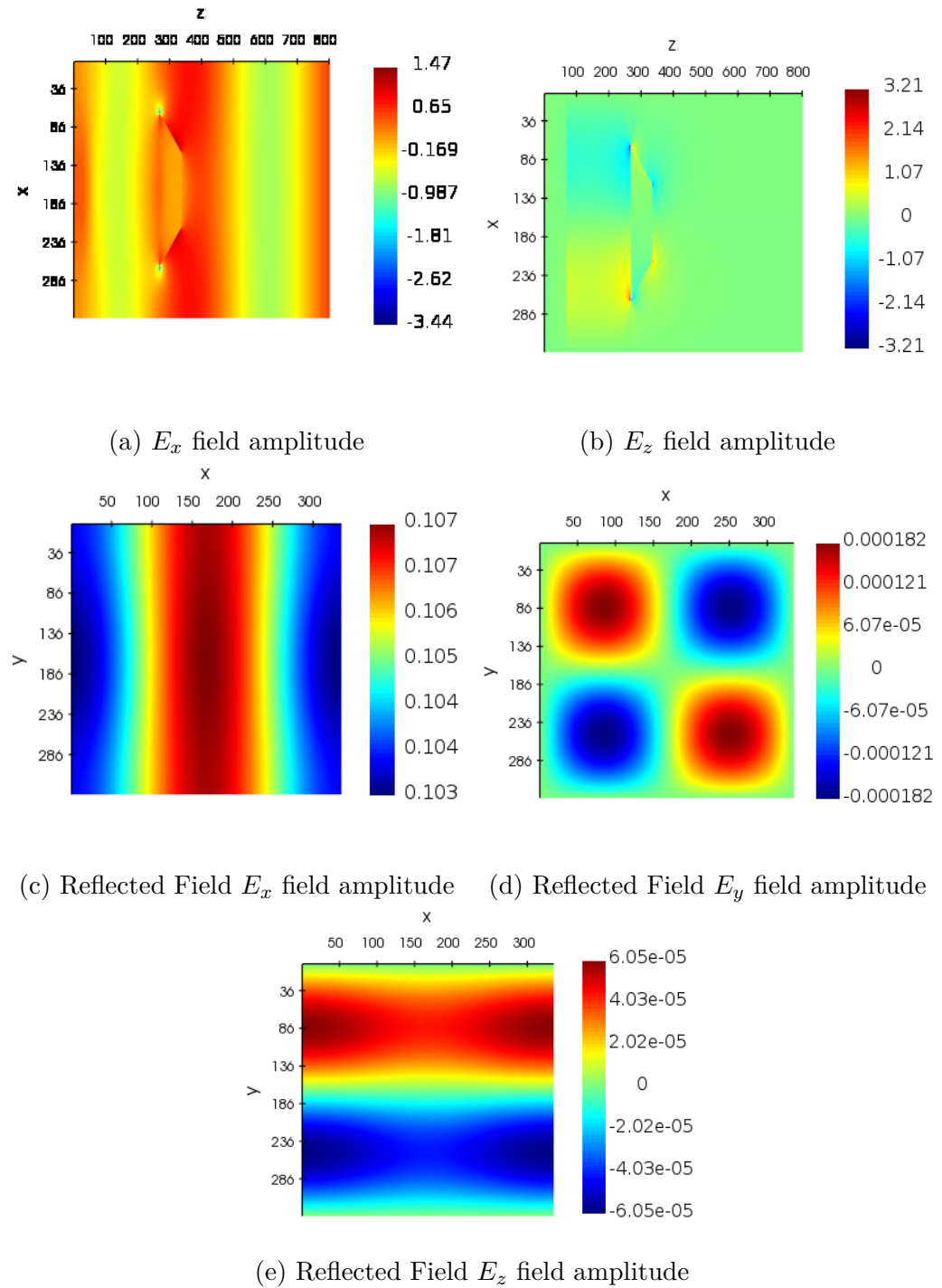
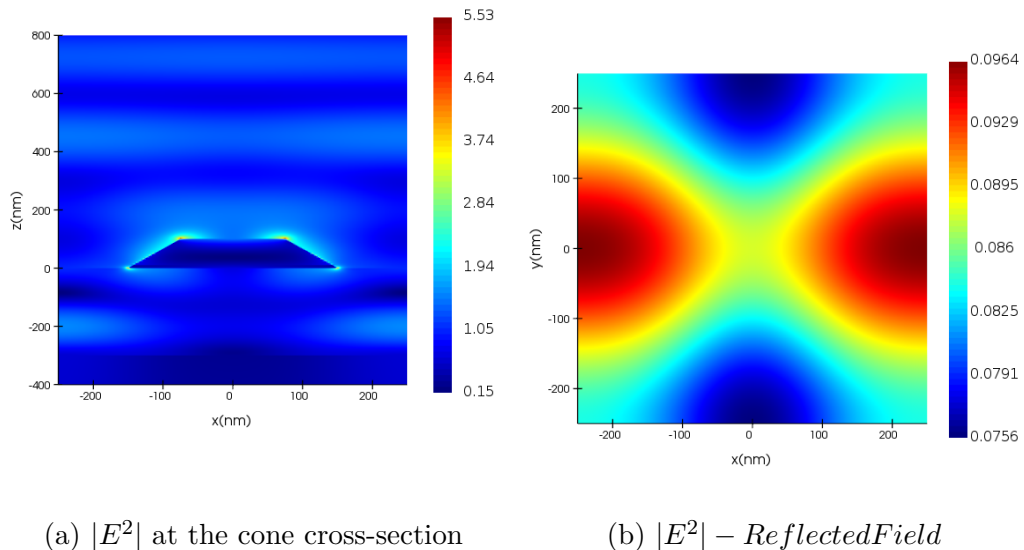


Figure 4.2: Cross-section field amplitude and reflected field amplitude at  $\lambda = 536\text{nm}$ .



(a)  $|E^2|$  at the cone cross-section

(b)  $|E^2| - \text{ReflectedField}$

Figure 4.3: Cross-section field intensity and reflected field intensity at  $\lambda = 536\text{nm}$ .

# Chapter 5

## Conclusion

We presented the theory required to understand and study defect SPEs in hBN. Starting from the properties of hBN and why it is a buzzing material for SPEs. We then presented the idea of confirming the presence of SPEs, i.e., via the  $g^{(2)}$  measurement. In the case of a 3 level defect states, we understood that the  $g^{(2)}$  for close lying ZPLs would have contributions from two decay times and thus would be different than a two-level system  $g^{(2)}$ . Further we also presented a 1D model to understand the PL spectrum and thus be able to distinguish between Group-1 and Group-2 SPEs in hBN through the introduction of the Huang-Rhys Factor. Our goal is to study the variation in SPEs with layer count, given they are strain activated defects. To do so, we visited a thin-plate theory model to understand the effect of strain on the bandstructure and thus an understanding of the corresponding spectra. This also allowed us to study the charge localisation based on Boltzmann statistics. We also performed FDTD simulations of a periodic nanocone structure with mesh convergence to study the field enhancement provided by the nanocones.

To achieve strain activated SPEs, we exfoliated monolayer hBN and characterised their nature. Onto nanofabricated Gold nanocones, we transferred the obtained hBN samples. The surface topography was studied using AFM, which gave us confirmation that hBN does conform to the Con nanostructures. Photoluminescence spectroscopy gave us confirmation on the emission and plasmonic effect of gold. We obtained a spectra which is a convolution of  $\sim 4$  peaks, of which we assume two are ZPLs and the other two the corresponding PSBs based on literature review. A power dependent PL study is performed, but results are inconclusive, since we require more data points to conclude saturation power values, as done in several other works.

Due to unavailability of experimental equipment, we couldn't perform the  $g^{(2)}$  and lifetime measurements for the samples, but the work is currently in progress. The nature of PL spectra provides positive feedback to the presence of defect based SPEs.

### 5.0.1 Future Work

- Perform  $g^{(2)}$  and excited state lifetime measurements for the sample.
- Study the effect of nanocone strain on multilayer hBN with a better model and compare the results with experiments.

# Bibliography

- [1] T. T. Tran, K. Bray, M. J. Ford, M. Toth, and I. Aharonovich, “Quantum emission from hexagonal boron nitride monolayers,” 2015.
- [2] G. Grynberg, A. Aspect, C. Fabre, and C. Cohen-Tannoudji, *Quantum description of light and its interaction with matter*, p. 299–300. Cambridge University Press, 2010.
- [3] M. D. Eisaman, J. Fan, A. Migdall, and S. V. Polyakov, “Invited review article: Single-photon sources and detectors,” *Review of Scientific Instruments*, vol. 82, no. 7, p. 071101, 2011.
- [4] H. Schauffert, J. C. Stewart, S. Ali, S. Walser, H. Hörner, A. S. Prasad, V. Babenko, Y. Fan, D. Eder, K. S. Thygesen, S. Hofmann, B. C. Bayer, and S. M. Skoff, “Characteristics of quantum emitters in hexagonal boron nitride suitable for integration with nanophotonic platforms,” 2022.
- [5] N. Mendelson, M. Doherty, M. Toth, I. Aharonovich, and T. T. Tran, “Strain-induced modification of the optical characteristics of quantum emitters in hexagonal boron nitride,” *Advanced Materials*, vol. 32, no. 21, p. 1908316, 2020.
- [6] G. Gross, H. Moon, B. Lienhard, S. Ali, D. K. Efetov, M. M. Furchi, P. Jarillo-Herrero, M. J. Ford, I. Aharonovich, and D. Englund, “Tunable and high-purity room temperature single-photon emission from atomic defects in hexagonal boron nitride,” *Nature Communications*, vol. 8, sep 2017.
- [7] A. Branny, S. Kumar, R. Proux, and B. D. Gerardot, “Deterministic strain-induced arrays of quantum emitters in a two-dimensional semiconductor,” *Nature Communications*, vol. 8, may 2017.
- [8] D. Wickramaratne, L. Weston, and C. G. Van de Walle, “Monolayer to bulk properties of hexagonal boron nitride,” *The Journal of Physical Chemistry C*, vol. 122, no. 44, pp. 25524–25529, 2018.
- [9] A. Sajid and K. Thygesen, “Vncb defect as source of single photon emission from hexagonal boron nitride,” *2D Materials*, vol. 7, no. 3, 2020.
- [10] A. L. Exarhos, D. A. Hopper, R. N. Patel, M. W. Doherty, and L. C. Bassett, “Magnetic-field-dependent quantum emission in hexagonal boron nitride at room temperature,” *Nature Communications*, vol. 10, no. 222, 2019.
- [11] N. Mendelson, Z.-Q. Xu, T. Tran, M. Kianinia, J. Scott, C. Bradac, I. Aharonovich, and M. Toth, “Engineering and tuning of quantum emitters in few-layer hexagonal boron nitride,” *ACS Nano*, vol. 13, 02 2019.

- [12] N. Mendelson, M. Doherty, M. Toth, I. Aharonovich, and T. T. Tran, “Strain engineering of quantum emitters in hexagonal boron nitride,” 2020.
- [13] L. Sortino, M. Brooks, P. G. Zotev, A. Genco, J. Cambiasso, S. Mignuzzi, S. A. Maier, G. Burkard, R. Sapienza, and A. I. Tartakovskii, “Dielectric nanoantennas for strain engineering in atomically thin two-dimensional semiconductors,” *ACS Photonics*, vol. 7, no. 9, pp. 2413–2422, 2020.
- [14] M. Brooks and G. Burkard, “Theory of strain-induced confinement in transition metal dichalcogenide monolayers,” *Phys. Rev. B*, vol. 97, p. 195454, May 2018.
- [15] R. V. Gorbachev, I. Riaz, R. R. Nair, R. Jalil, L. Britnell, B. D. Belle, E. W. Hill, K. S. Novoselov, K. Watanabe, T. Taniguchi, A. K. Geim, and P. Blake, “Hunting for monolayer boron nitride: Optical and raman signatures,” *Small*, vol. 7, no. 4, pp. 465–468, 2011.
- [16] A. P. Hard, S. F. Parker, and U. A. Jayasooriya, “Vibrational spectroscopic analysis of chlorosilanes and siloxane oligomers: Implications for the spectra of polydimethylsiloxanes,” *Applied Spectroscopy*, vol. 61, no. 3, pp. 314–320, 2007. PMID: 17389072.
- [17] P. A. Atanasov, N. E. Stankova, N. N. Nedyalkov, T. R. Stoyanchoff, R. G. Nikov, N. Fukata, J. W. Gerlach, D. Hirsch, and B. Rauschenbach, “Properties of ns-laser processed polydimethylsiloxane (pdms),” *Journal of Physics: Conference Series*, vol. 700, p. 012023, mar 2016.
- [18] J. Wang, F. Ma, and M. Sun, “Graphene, hexagonal boron nitride, and their heterostructures: properties and applications,” *RSC Adv.*, vol. 7, pp. 16801–16822, 2017.
- [19] Q. Cai, D. Scullion, A. Falin, K. Watanabe, T. Taniguchi, Y. Chen, E. J. G. Santos, and L. H. Li, “Raman signature and phonon dispersion of atomically thin boron nitride,” *Nanoscale*, vol. 9, pp. 3059–3067, 2017.
- [20] Z. Shotan, H. Jayakumar, C. R. Considine, M. Mackoit, H. Fedder, J. Wrachtrup, A. Alkauskas, M. W. Doherty, V. M. Menon, and C. A. Meriles, “Photoinduced modification of single-photon emitters in hexagonal boron nitride,” *ACS Photonics*, vol. 3, no. 12, pp. 2490–2496, 2016.
- [21] A. Slachter, “Single photon emitters and their use in quantum cryptography and quantum computing,”
- [22] I. Aharonovich, D. Englund, and M. Toth, “Solid-state single-photon emitters,” *Nature Photonics*, vol. 10, pp. 631–641, Oct 2016.
- [23] N. V. Proscia, Z. Shotan, H. Jayakumar, P. Reddy, C. Cohen, M. Dollar, A. Alkauskas, M. Doherty, C. A. Meriles, and V. M. Menon, “Near-deterministic activation of room-temperature quantum emitters in hexagonal boron nitride,” *Optica*, vol. 5, pp. 1128–1134, Sep 2018.
- [24] G. Ballesteros, R. Proux, C. Bonato, and B. Gerardot, “readPTU: a python library to analyse time tagged time resolved data,” *Journal of Instrumentation*, vol. 14, pp. T06011–T06011, jun 2019.

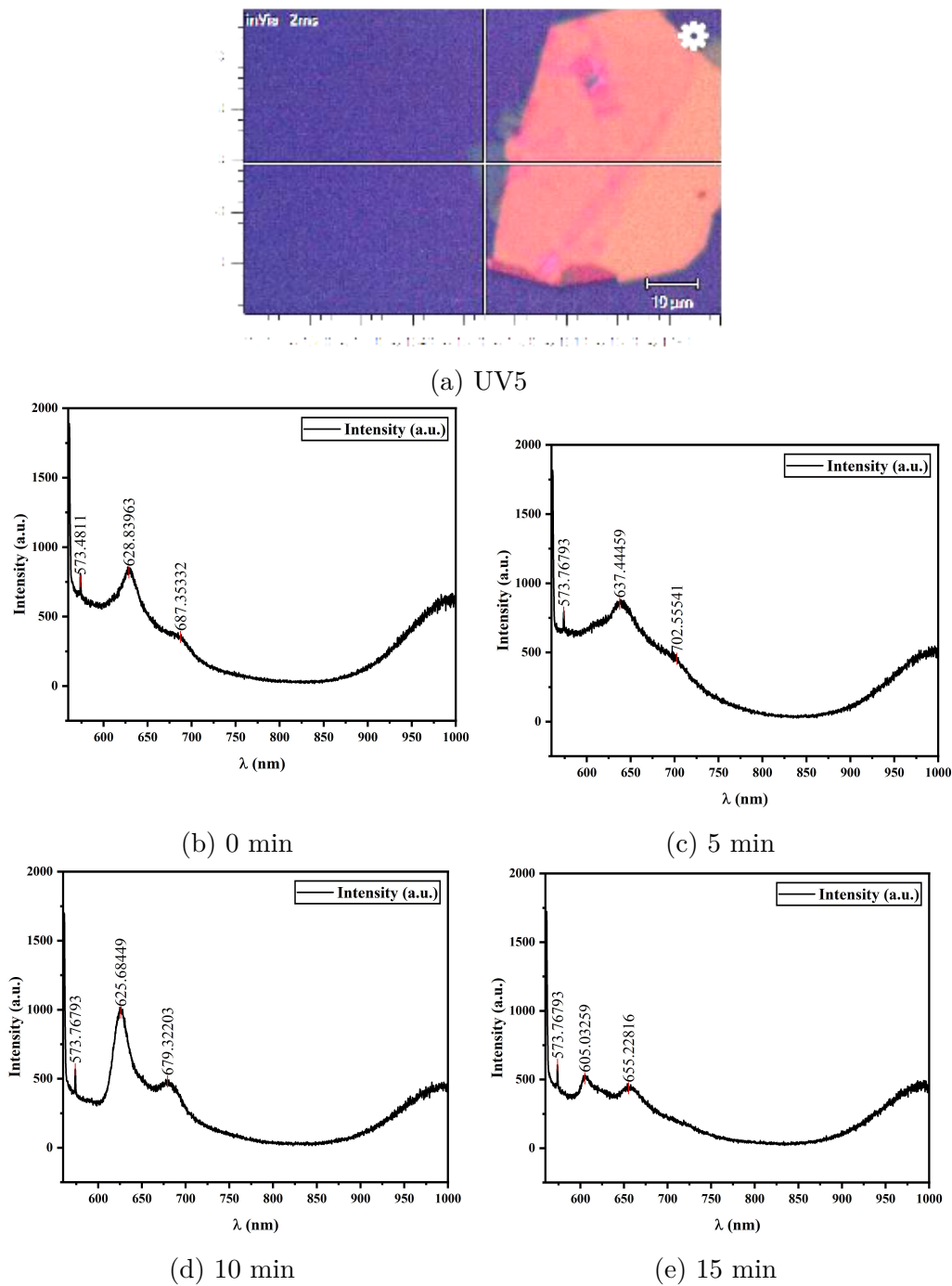
# **Appendix A**

## **Further Work**

### **A.0.1 UV-Ozone Treatment**

The idea of strain activated defects was established earlier. However, this is not the only way to create/activate deep defect states that allow for photoemission. UV-Ozone treatment is one such method.

Here, the treatment creates defect states due to the highly reactive nature of Ozone, thus generating photoemission states. We performed the treatment 3 times, on the same sample for 5 mins each, and recorded the PL spectrum at the same location after each treatment. The results are presented below.



### A.0.2 Reflectance Spectrum

We performed the reflectance spectroscopy of the Gold nanocones. We studied the effect of hBN on the cone's reflectivity. The reflectance spectra is presented below.

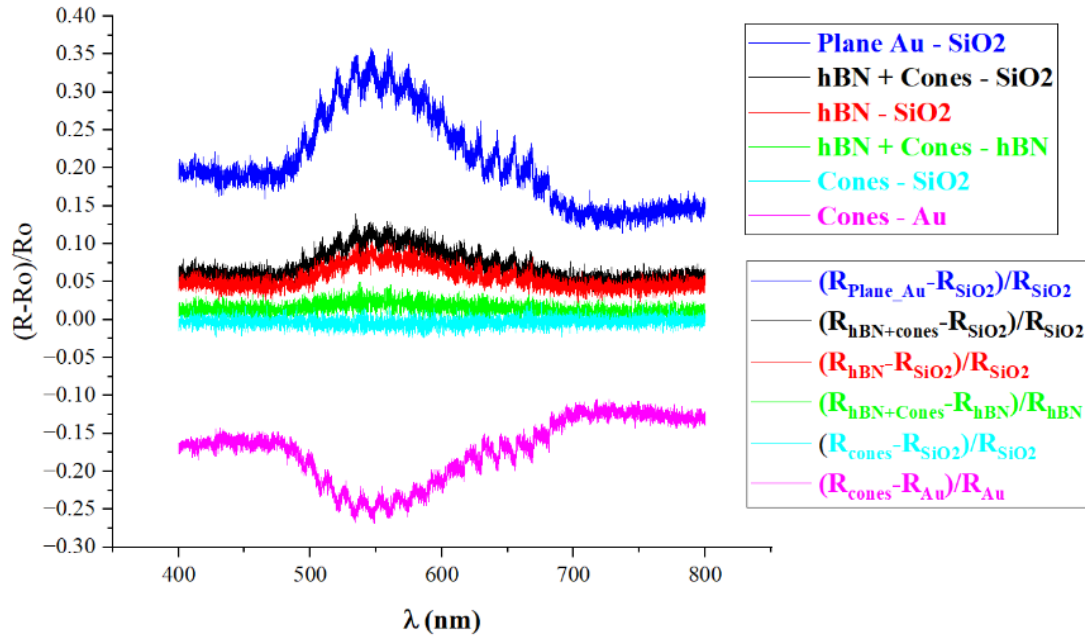


Figure A.2: Reflectance Spectra